Monthly Notices
of the
ROYAL ASTRONOMICAL SOCIETY

MNRAS **464,** 1640–1658 (2017)
Advance Access publication 2016 September 28

doi:10.1093/mnras/stw2443

The clustering of galaxies in the completed SDSS-III Baryon Oscillation Spectroscopic Survey: Cosmological implications of the configuration-space clustering wedges

Ariel G. Sánchez,[1⋆] Román Scoccimarro,[2] Martín Crocce,[3] Jan Niklas Grieb,[1,4] Salvador Salazar-Albornoz,[1,4] Claudio Dalla Vecchia,[5,6] Martha Lippich,[1,4] Florian Beutler,[7,8] Joel R. Brownstein,[9] Chia-Hsun Chuang,[10,11] Daniel J. Eisenstein,[12] Francisco-Shu Kitaura,[8,11,13] Matthew D. Olmstead,[14] Will J. Percival,[7] Francisco Prada,[10,15,16] Sergio Rodríguez-Torres,[10,15,17] Ashley J. Ross,[7,18] Lado Samushia,[7,19,20] Hee-Jong Seo,[21] Jeremy Tinker,[2] Rita Tojeiro,[22] Mariana Vargas-Magaña,[23,24,25] Yuting Wang[7,26] and Gong-Bo Zhao[7,26]

Affiliations are listed at the end of the paper

Accepted 2016 September 26. Received 2016 September 21; in original form 2016 July 11

ABSTRACT

We explore the cosmological implications of anisotropic clustering measurements in configuration space of the final galaxy samples from Data Release 12 of the Sloan Digital Sky Survey III Baryon Oscillation Spectroscopic Survey. We implement a new detailed modelling of the effects of non-linearities, bias and redshift-space distortions that can be used to extract unbiased cosmological information from our measurements for scales $s \gtrsim 20\,h^{-1}$ Mpc. We combined the information from Baryon Oscillation Spectroscopic Survey (BOSS) with the latest cosmic microwave background (CMB) observations and Type Ia supernovae samples and found no significant evidence for a deviation from the Λ cold dark matter (ΛCDM) cosmological model. In particular, these data sets can constrain the dark energy equation-of-state parameter to $w_{\rm DE} = -0.996 \pm 0.042$ when to be assumed time independent, the curvature of the Universe to $\Omega_k = -0.0007 \pm 0.0030$ and the sum of the neutrino masses to $\sum m_\nu < 0.25$ eV at 95 per cent confidence levels. We explore the constraints on the growth rate of cosmic structures assuming $f(z) = \Omega_{\rm m}(z)^\gamma$ and obtain $\gamma = 0.609 \pm 0.079$, in good agreement with the predictions of general relativity of $\gamma = 0.55$. We compress the information of our clustering measurements into constraints on the parameter combinations $D_{\rm V}(z)/r_{\rm d}$, $F_{\rm AP}(z)$ and $f\sigma_8(z)$ at $z_{\rm eff} = 0.38$, 0.51 and 0.61 with their respective covariance matrices and find good agreement with the predictions for these parameters obtained from the best-fitting ΛCDM model to the CMB data from the *Planck* satellite. This paper is part of a set that analyses the final galaxy clustering data set from BOSS. The measurements and likelihoods presented here are combined with others by Alam et al. to produce the final cosmological constraints from BOSS.

Key words: cosmological parameters – large-scale structure of Universe.

1 INTRODUCTION

Measurements of the large-scale clustering of galaxies offer a powerful route to obtain accurate cosmological information (Davis & Peebles 1983; Maddox et al. 1990; Tegmark et al. 2004; Cole et al. 2005; Eisenstein et al. 2005; Anderson et al. 2012, 2014a,b). Two-point statistics such as the power spectrum, $P(k)$, and its Fourier transform, the two-point correlation function $\xi(s)$, have been the preferred tools for analyses of the large-scale structure (LSS) of the Universe. The shape of these measurements can be used to constrain the values of several cosmological parameters, providing

⋆ E-mail: arielsan@mpe.mpg.de

clues about the nature of dark energy, potential deviations from the predictions of general relativity (GR), the physics of inflation, neutrino masses, etc. (Percival et al. 2002, 2010; Tegmark et al. 2004; Sánchez et al. 2006, 2009, 2012; Blake et al. 2011; Parkinson et al. 2012).

A particularly important source of cosmological information contained in the large-scale galaxy clustering pattern is the signature of the baryon acoustic oscillations (BAO), which are the vestige of acoustic waves that propagated through the photon–baryon fluid prior to recombination. The BAO signature was first detected by Eisenstein et al. (2005) in the correlation function of the luminous red galaxy sample of the Sloan Digital Sky Survey (SDSS; York et al. 2000), where it can be seen as a broad peak on large scales (Matsubara 2004), and by Cole et al. (2005) in the power spectrum of the

Two-degree Field Galaxy Redshift survey (Colless et al. 2001, 2003), where it appears as a series of wiggles (Eisenstein & Hu 1998; Meiksin, White & Peacock 1999). The position of the peak in the correlation function and the wavelength of the oscillations in the power spectrum closely match the sound horizon scale at the drag redshift, $r_{\rm d} \simeq 150\,{\rm Mpc}$. This means that the BAO scale inferred from the clustering of galaxies in the directions parallel and perpendicular to the line of sight can be used as a standard ruler to measure the Hubble parameter, $H(z)$, and the angular diameter distance, $D_{\rm M}(z)$, through the Alcock–Paczynski (AP) test (Alcock & Paczynski 1979; Blake & Glazebrook 2003; Linder 2003).

As the AP test cannot be applied to angle-averaged clustering measurements, the full power of the BAO signal can only be exploited by means of anisotropic clustering measurements. That means measurements of the full two-dimensional correlation function or power spectrum (Wagner, Müller & Steinmetz 2008; Shoji, Jeong & Komatsu 2009), their Legendre multipole moments (Padmanabhan & White 2008) or the clustering wedges statistic (Kazin, Sánchez & Blanton 2012). These measurements are affected by redshift-space distortions (RSD) due to the peculiar velocities of the galaxies along the line of sight, which are significantly larger than the geometric distortions due to the AP effect and must be accurately modelled to avoid introducing systematic errors in the obtained constraints. However, more than a complication for the application of the AP test, RSD provide additional cosmological information, as they can be used to constrain the growth rate of cosmic structures (Guzzo et al. 2008). In this way, thanks to the joint information from BAO and RSD, anisotropic clustering measurements can provide information on the expansion history of the Universe and the growth rate of density fluctuations, which is essential to distinguish between dark energy and modified gravity as the driver of cosmic acceleration.

Previous analyses of anisotropic clustering measurements based on data from the SDSS-III (Eisenstein et al. 2011) Baryon Oscillation Spectroscopic Survey (BOSS; Dawson et al. 2013), clearly illustrated their constraining power (Anderson et al. 2014a,b; Reid et al. 2012; Chuang et al. 2013; Samushia et al. 2013, 2014; Beutler et al. 2014). In particular, Sánchez et al. (2013, 2014) explored the cosmological implications of the full shape of measurements of two clustering wedges based on the galaxy samples of BOSS Data Release 11 (DR11). In this paper, we extend these analyses to the final galaxy samples from BOSS, corresponding to SDSS DR12 (Alam et al. 2015). The volume probed by DR12 is only ∼10 per cent larger than that of DR11. For this reason, we focus on improving our analysis methodology in order to maximize the cosmological information extracted from the sample. We make use of the joint information of the LOWZ and CMASS galaxy samples into the *combined* BOSS sample described in Reid et al. (2016), increasing the effective volume of the survey with respect to the separate analysis of these samples (Alam et al. 2016). We also use state-of-the-art models of the effect of non-linearities, bias and RSDs that allow us to extend our analysis of the full shape of the clustering wedges to smaller scales. We perform extensive tests of the performance of our methodology on *N*-body simulations and mock catalogues and find precise and accurate constraints.

Our analysis is part of a series of papers examining the information in the anisotropic clustering pattern of the combined sample of BOSS DR12. Salazar-Albornoz et al. (2016) perform a tomographic analysis of the clustering properties of this sample by means of angular correlation functions in thin redshift shells. Grieb et al. (2016b) use the same description of non-linearities, bias and RSD used in our analysis to extract cosmological information from the full shape of three clustering wedges measured in Fourier space. Satpathy et al. (2016) use a model based on convolution Lagrangian perturbation theory (Carlson, Reid & White 2013; Wang, Reid & White 2014) and the Gaussian streaming model (Scoccimarro 2004; Reid & White 2011) to fit the full shape of the monopole and quadrupole of the two-point correlation function, $\xi_{0,2}(s)$. Beutler et al. (2016a) apply a model based on Taruya, Nishimichi & Saito (2010) to the power spectrum multipoles $P_\ell(k)$ for $\ell = 0, 2, 4$. Tinker et al. (in preparation) present a comparison of the results of different RSD analysis techniques. Ross et al. (2016) and Beutler et al. (2016b) perform BAO-only fits to the Legengre multipoles of order $\ell = 0, 2$ of the two-point functions in configuration and Fourier space obtained after the application of the reconstruction technique (Eisenstein et al. 2007; Padmanabhan et al. 2012) as described in Cuesta et al. (2016). The potential systematics of these BAO-only measurements are discussed in Vargas-Magaña et al. (2016). Alam et al. (2016) use the methodology described in Sánchez et al. (2016) to combine the results presented here with those of the other full-shape and BAO-only analyses into a final set of BOSS consensus constraints and explore their cosmological implications.

The outline of this paper is as follows. In Section 2, we describe our galaxy sample, the procedure we follow to measure the clustering wedges and the mock catalogues used to compute our estimate of their covariance matrices. Our model of the full shape of the clustering wedges is described in Section 3.1, together with the tests we have performed by applying it to *N*-body simulations and mock catalogues. In Section 4, we study the cosmological implications of our clustering measurements. After describing our methodology to obtain cosmological constraints in Section 4.1, Sections 4.2–4.6 describe the results we obtained from different combinations of data sets and parameter spaces. In Section 5, we compress the information of the BOSS clustering wedges into geometric constraints and measurements of the growth of structure. Finally, we present our main conclusions in Section 6.

2 THE BARYON OSCILLATION SPECTROSCOPIC SURVEY

2.1 Galaxy clustering measurements from BOSS

We use the final galaxy samples of BOSS, corresponding to SDSS DR12 (Alam et al. 2015). The catalogue is divided into two samples, called LOWZ and CMASS, which were selected on the basis of the SDSS multicolour photometric observations (Gunn et al. 1998, 2006) to cover the redshift range $0.15 < z < 0.7$ with a roughly uniform comoving number density $n \simeq 3 \times 10^{-4}\,h^3\,{\rm Mpc}^{-3}$ (Eisenstein

et al. 2011; Dawson et al. 2013). After identifying the galaxies with previous spectroscopic observations from the SDSS I/II surveys (York et al. 2000), the remaining redshifts were measured from the spectra obtained with the BOSS spectrographs (Smee et al. 2013) as described in Aihara et al. (2011) and Bolton et al. (2012).

The CMASS sample is approximately complete down to a limiting stellar mass of $M \simeq 10^{11.3}\,\mathrm{M}_{\odot}$ for $z > 0.45$ (Maraston et al. 2013), with an ∼10 per cent satellite fraction (White et al. 2011; Nuza et al. 2013). Although it is dominated by early-type galaxies, ∼26 per cent of this sample consist of massive spirals showing star formation activity in their spectra (Masters et al. 2011; Thomas et al. 2013). The LOWZ sample consists primarily of red galaxies located in massive haloes, and has ∼12 per cent satellite fraction (Parejko et al. 2013). As described in Reid et al. (2016), a few regions of the LOWZ sample in the Northern Galactic Cap (NGC) were targeted using different photometric cuts, leading to a reduction of the galaxy number density. The obtained galaxy samples, which cover approximately 1000 deg^2, are labelled LOWZE2 and LOWZE3.

Previous clustering analyses of BOSS data have made use of the LOWZ and CMASS samples separately, excluding the LOWZE2 and LOWZE3 regions. Here, we use the full BOSS data set by combining all these samples as described in Reid et al. (2016). We follow Alam et al. (2016) and split this combined sample into three overlapping redshift bins of roughly equal volume defined by $0.2 < z < 0.5$, $0.4 < z < 0.6$ and $0.5 < z < 0.75$.

We study the clustering properties of the combined BOSS galaxy sample by means of the clustering wedges statistic (Kazin et al. 2012), $\xi^{\mu_2}_{\mu_1}(s)$, which corresponds to the average of the full two-dimensional correlation function $\xi(\mu, s)$, where μ is the cosine of the angle between the separation vector $\boldsymbol{s}$ and the line-of-sight direction, over the interval $\Delta\mu = \mu_2 - \mu_1$, that is,

$$\xi^{\mu_2}_{\mu_1}(s) \equiv \frac{1}{\Delta\mu}\int_{\mu_1}^{\mu_2} \xi(\mu, s)\,\mathrm{d}\mu. \tag{1}$$

Sánchez et al. (2013, 2014) used two wide clustering wedges, dividing the μ range from 0 to 1 into two equal-width intervals. Here, we measure three wedges, which we denote by $\xi_{3\mathrm{w}}(s)$ and refer to each individual wedge as $\xi_{3\mathrm{w},\,i}(s)$ for the intervals $(i-1)/3 < \mu < i/3$. In practice, the value of μ of a given galaxy pair is estimated as the cosine of the angle between the separation vector, $\boldsymbol{s}$, and the line-of-sight direction at the mid-point of $\boldsymbol{s}$.

The observed galaxy redshifts are converted into distances using the same fiducial cosmology as in our companion papers, a flat Λ cold dark matter (ΛCDM) model with a matter density parameter $\Omega_{\mathrm{m}} = 0.31$. This choice is taken into account in our modelling as described in Section 3.2. We compute the full two-dimensional correlation function $\xi(\mu, s)$ of the combined sample in each redshift bin using the estimator of Landy & Szalay (1993). We employ a random catalogue following the same angular and radial selection function as the combined sample but containing 50 times more objects. We compute the clustering wedges by averaging the full $\xi(\mu, s)$ over the corresponding μ intervals. As in our companion papers, we use a bin size of $\mathrm{d}s = 5\,h^{-1}$ Mpc.

We assign a series of weights to each object in our galaxy and random catalogues. First, we apply a weight designed to minimize the variance of our measurements (Feldman, Kaiser & Peacock 1994) given by

$$w_{\mathrm{r}}(\boldsymbol{x}) = \frac{1}{1 + P_w \bar{n}(\boldsymbol{x})}, \tag{2}$$

where $\bar{n}(\boldsymbol{x})$ is the expected number density of the catalogue at a given position $\boldsymbol{x}$ and P_w is a scale-independent parameter, which we set to $P_w = 10^4\,h^{-3}\,\mathrm{Mpc}^3$. This choice is motivated by the fact that this value is close to the amplitude of the BOSS power spectrum at $k = 0.14\,h\,\mathrm{Mpc}^{-1}$, which is the effective scale suggested by Font-Ribera et al. (2014) to use for BOSS BAO measurements. The galaxy catalogue also includes weights to account for redshift failures and fibre collisions. The LOWZE2, LOWZE3 and CMASS samples require additional weights to correct for the systematic effect introduced by the local stellar density and the seeing of the observations, as described in detail in Ross et al. (2016). Fig. 1 shows the resulting wedges $\xi_{3\mathrm{w}}(s)$ of the DR12 combined sample in our three redshift bins as a function of the pair separation expressed in Mpc and Mpc h^{-1} in the lower and upper axes, respectively. These measurements and their corresponding covariance matrices (see Section 2.2) are publicly available.[1] The signature of the BAO is clearly visible in all wedges at $s \simeq 150$ Mpc. The anisotropic clustering pattern generated by RSDs leads to significant differences in the amplitude and shape of the three wedges. The solid lines in the same figure correspond to the best-fitting models obtained as described in Section 5.

2.2 Covariance matrix estimation

We assume a Gaussian likelihood function for our BOSS clustering measurements given by

$$-2\ln\mathcal{L}(\boldsymbol{\xi}|\boldsymbol{\theta}) = \left(\boldsymbol{\xi} - \boldsymbol{\xi}_{\mathrm{theo}}(\boldsymbol{\theta})\right)^t \Psi \left(\boldsymbol{\xi} - \boldsymbol{\xi}_{\mathrm{theo}}(\boldsymbol{\theta})\right), \tag{3}$$

where $\boldsymbol{\xi}$ is an array containing the measured clustering wedges and $\boldsymbol{\xi}_{\mathrm{theo}}(\boldsymbol{\theta})$ corresponds to our theoretical modelling of these data for the cosmological parameters $\boldsymbol{\theta}$. The evaluation of the likelihood function requires the knowledge of the inverse of the covariance matrix, $\Psi = \mathbf{C}^{-1}$, also known as the precision matrix, which we estimate using the MULTIDARK-PATCHY(MD-PATCHY) BOSS mock galaxy catalogues described in Kitaura et al. (2016a). These mocks consist of a set of $N_{\mathrm{m}} = 2045$ independent realizations of the final BOSS combined sample, corresponding to the best-fitting ΛCDM cosmology to the Planck 2013 cosmic microwave background (CMB) measurements (Planck Collaboration XVI 2014). We computed the wedges $\xi_{3\mathrm{w}}(s)$ of each mock catalogue in the same way as for the real BOSS data, and used these measurements to obtain an estimate of the full covariance matrix $\hat{\mathbf{C}}$ of our clustering measurements. The error bars in Fig. 1 correspond to the square root of the diagonal entries of $\hat{\mathbf{C}}$.

As a test of the robustness of our results with respect to the details in the estimation of the covariance matrix, we also used an independent set of 1000 Quick Particle Mesh (QPM; White, Tinker & McBride 2014) mock realizations of the BOSS combined sample. The covariance matrices inferred from the QPM and MD-PATCHY mocks are consistent and lead to similar results. However, as the MD-PATCHY mock samples give a somewhat better match to the clustering properties of the BOSS combined sample than QPM (Kitaura et al. 2016a) and have a significantly larger number of realizations, we based our final constraints on the covariance matrices inferred from these mock catalogues.

Our estimates of the covariance matrix are affected by sampling noise due to the finite number of mock catalogues. Recent studies have provided a clear description of the dependence of the noise in the estimated covariance matrix on the number of mock catalogues

[1] https://www.sdss3.org/science/boss_publications.php

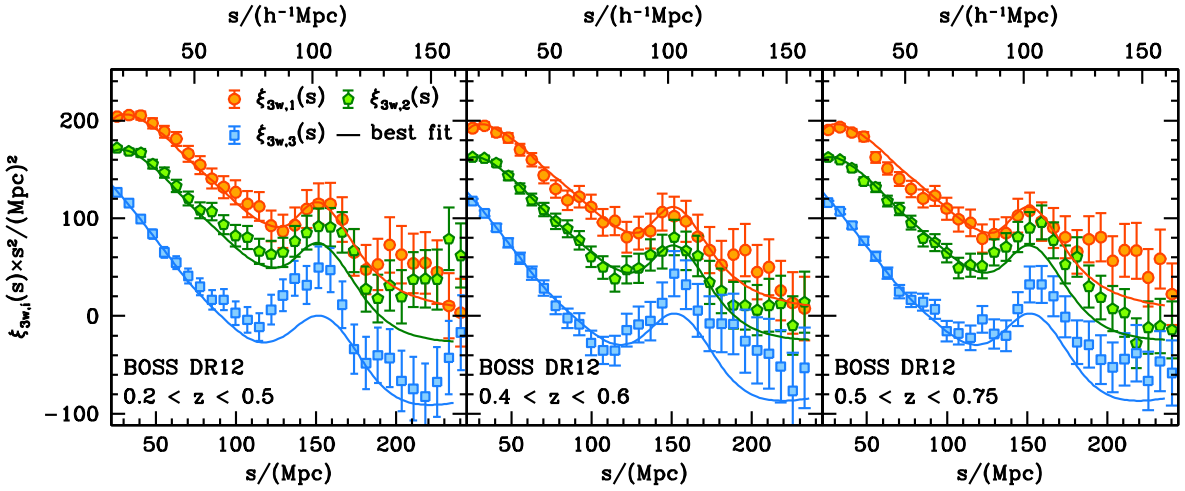

Figure 1. Clustering wedges in the directions parallel (blue) intermediate (green) and transverse (red) to the line of sight measured from the combined galaxy sample of BOSS DR12 in our three redshift bins, as a function of the pair separation expressed in Mpc and h^{-1} Mpc in the lower and upper axes, respectively. The error bars correspond to the dispersion of the results inferred from a set of $N_{\rm m} = 2045$ mock catalogues of the full BOSS survey. The solid lines correspond to the best-fitting model to these measurements obtained as described in Section 5.

used (Taylor, Joachimi & Kitching 2013), its propagation to the derived parameter uncertainties (Dodelson & Schneider 2013; Taylor & Joachimi 2014) and the correct way to include this additional uncertainty in the obtained constraints (Percival et al. 2014).

The first effect that must be taken into account is that when the covariance matrix is estimated from a set of independent realizations, the uncertainties in $\hat{\mathbf{C}}$ and its inverse follow the Wishart and inverse-Whishart distributions (Wishart 1928), respectively. As the inverse-Whishart distribution is asymmetric, the inverse of $\hat{\mathbf{C}}$ provides a biased estimate of Ψ. This can be corrected for by including a prefactor in the estimate of the precision matrix as (Kaufman 1967; Hartlap, Simon & Schneider 2007)

$$\hat{\Psi} = \left(1 - \frac{N_{\rm b} + 1}{N_{\rm m} - 1}\right) \hat{\mathbf{C}}^{-1}, \tag{4}$$

where $N_{\rm b}$ corresponds to the total number of bins in our measurements. We restrict our analysis to $20\,h^{-1}$ Mpc $< s < 160\,h^{-1}$ Mpc with a bin-width of $\mathrm{d}s = 5\,h^{-1}$ Mpc, leading to $N_{\rm b} = 84$ for our three clustering wedges. As our estimates of the covariance matrix are based on the $N_{\rm m} = 2045$ MD-PATCHY mock catalogues, the factor of equation (4) is equal to 0.96.

Although the estimate of the precision matrix $\hat{\Psi}$ of equation (4) is unbiased, it is still affected by noise, which should be propagated into the obtained cosmological constraints. Percival et al. (2014) derived formulae for their impact on the errors of the cosmological constraints measured by integrating over the likelihood function. They demonstrated that, to account for this extra uncertainty, the recovered parameter constraints must be rescaled by a factor that depends on $N_{\rm b}$, $N_{\rm m}$ and the number of parameters included in the analysis, $N_{\rm p}$ (see equation 18 in Percival et al. 2014). Depending on the parameter space, our choice of range of scales and binning leads to a modest correction factor of at most 1.6 per cent for the results inferred from the clustering wedges. The additional uncertainty due to the finite number of mock catalogues could be reduced by implementing techniques such as covariance tapering (Paz & Sánchez 2015) but, as the impact on our constraints is small, we simply include the correction factor of Percival et al. (2014) in our results.

3 THE MODEL

3.1 Modelling non-linear gravitational evolution, bias and RSD

The prediction of the clustering wedges for a given cosmology requires a model of the full two-dimensional correlation function $\xi(\mu, s)$. It is convenient to express $\xi(\mu, s)$ as a linear combination of Legendre polynomials, $L_\ell(\mu)$, as

$$\xi(\mu, s) = \sum_{\text{even } \ell} L_\ell(\mu)\xi_\ell(s), \tag{5}$$

where the multipoles $\xi_\ell(s)$ are given by

$$\xi_\ell(s) \equiv \frac{2\ell + 1}{2} \int_{-1}^{1} L_\ell(\mu)\xi(\mu, s)\,\mathrm{d}\mu. \tag{6}$$

In order to obtain a description of the multipoles $\xi_\ell(s)$, it is useful to work with the two-dimensional power spectrum, $P(\mu, k)$. This quantity can also be decomposed in terms of Legendre polynomials, with multipoles given by

$$P_\ell(k) \equiv \frac{2\ell + 1}{2} \int_{-1}^{1} L_\ell(\mu)P(\mu, k)\,\mathrm{d}\mu, \tag{7}$$

from which the multipoles $\xi_\ell(s)$ can be obtained as

$$\xi_\ell(s) \equiv \frac{i^\ell}{2\pi^2} \int_0^\infty P_\ell(k) j_\ell(ks)\, k^2 \mathrm{d}k, \tag{8}$$

where $j_\ell(x)$ is the spherical Bessel function of order ℓ.

An accurate model of the full shape of $P(\mu, k)$ must take into account the effects of the non-linear evolution of density fluctuations, galaxy bias and RSD. We now describe how each of these distortions is taken into account in our model.

3.1.1 *Non-linear dynamics*

The accurate modelling of the effects of the non-linear evolution of density fluctuations has been the focus of significant work over the last decade or so. In renormalized perturbation theory (RPT; Crocce & Scoccimarro 2006) and subsequent developments in terms of the multipoint propagator expansion (Bernardeau, Crocce

& Scoccimarro 2008, 2012; Crocce, Scoccimarro & Bernardeau 2012; Taruya et al. 2012; Taruya, Nishimichi & Bernardeau 2013; Bernardeau, Taruya & Nishimichi 2014), the matter power spectrum is written as

$$P_{\rm NL}(k) = P_{\rm L}(k)\, G(k)^2 + P_{\rm MC}(k), \tag{9}$$

where the propagator $G(k)$ corresponds to a resummation of all the terms in the perturbation expansion that are proportional to the linear spectrum $P_{\rm L}(k)$, and $P_{\rm MC}(k)$ contains mode-coupling contributions (which at N loops involve convolutions over N linear spectra). To an excellent approximation for CDM spectra, the propagator describes the damping of the BAO, while the mode-coupling power describes the shift of the BAO scale (Crocce & Scoccimarro 2008; Seo et al. 2010). Using e.g. the one-loop approximation to the mode-coupling power in this approach has a limited reach in k (see e.g. Crocce et al. 2012), which is mainly set by the breaking of Galilean invariance (Scoccimarro & Frieman 1996) due to the fact that the propagator is resummed while the mode-coupling power is not. Here, we follow the approach of Crocce, Blas & Scoccimarro (in preparation), who uses Galilean invariance to find a resummation of the mode-coupling power consistent with the resummation of the propagator. With this approach, dubbed gRPT, it is possible to obtain an improved description down to smaller scales, $k \lesssim 0.25\, h\,{\rm Mpc}^{-1}$ for the uncertainties involved in our measurements, see Section 3.3.

3.1.2 Galaxy bias

To describe the clustering of galaxies, we write the bias relation between the matter density fluctuations δ and the galaxy density fluctuations, $\delta_{\rm g}$, as in Chan, Scoccimarro & Sheth (2012)

$$\delta_{\rm g} = b_1\delta + \frac{b_2}{2}\delta^2 + \gamma_2\,\mathcal{G}_2 + \gamma_3^-\,\Delta_3\mathcal{G} + \cdots, \tag{10}$$

where at cubic order the only term that contributes to the one-loop galaxy power spectrum through the first two multipoint propagators has been written down. The operators $\mathcal{G}_2$ and $\Delta_3\mathcal{G}$ are defined as

$$\mathcal{G}_2(\Phi_v) = (\nabla_{ij}\Phi_v)^2 - (\nabla^2\Phi_v)^2, \tag{11}$$

and

$$\Delta_3\mathcal{G} = \mathcal{G}_2(\Phi) - \mathcal{G}_2(\Phi_v), \tag{12}$$

where Φ and Φ_v are the normalized density and velocity potentials $\nabla^2\Phi = \delta$ and $\nabla^2\Phi_v = \theta$.

A few points about the bias relation in equation (10) are worth making here. First, under local Lagrangian bias, the non-local bias parameters are related to the linear bias b_1 as (Fry 1996; Catelan et al. 1998; Catelan, Porciani & Kamionkowski 2000; Chan et al. 2012)

$$\gamma_2 = -\frac{2}{7}(b_1 - 1), \tag{13}$$

$$\gamma_3^- = \frac{11}{42}(b_1 - 1). \tag{14}$$

Secondly, while there is no compelling argument for the validity of local Lagrangian bias (Sheth, Chan & Scoccimarro 2013), a bispectrum analysis of dark matter haloes shows that the $\gamma_2(b_1)$ relation in equation (13) is at least a reasonable first approximation (Baldauf et al. 2012; Chan et al. 2012; Sheth et al. 2013; Saito et al. 2014; Bel, Hoffmann & Gaztañaga 2015). In our context here this is particularly relevant given that in this work we use two-point statistics alone, which do not constrain γ_2 that well. Therefore, we assume the $\gamma_2(b_1)$ relation in equation (13). We have in fact checked relaxing this assumption, using CMASS-type galaxies in the MINERVA simulations (discussed below), and it does not bias our results.

Finally, the situation is somewhat different for the γ_3^- parameter, and we *do not* assume the $\gamma_3^-(b_1)$ relation in equation (14) for a number of reasons. First, the linear bias b_1 is the only bias parameter that receives significant signal to noise over a broad range of scales, as opposed to the rest of the terms in equation (10) that only enter through loop corrections for our two-point function only analysis. Therefore, one should in principle include the running of b_1 with scale, which corresponds to adding a $\nabla^2\delta$ term in equation (10). However, such term is fairly degenerated with the contribution coming from γ_3^- (McDonald & Roy 2009; Biagetti et al. 2014; Saito et al. 2014), and thus provided we let γ_3^- (and b_2 as well) be free one can absorb such contributions given the range of scales considered in our analysis. The same holds for stress tensor contributions to dark matter clustering (Pueblas & Scoccimarro 2009; Baumann et al. 2012; Carrasco, Hertzberg & Senatore 2012; Pietroni et al. 2012) that are fully degenerated with the running of the linear bias.

Summarizing, our bias model has three free parameters corresponding to b_1, b_2, γ_3^-, with γ_2 given in terms of b_1 by the local Lagrangian bias relation in equation (13). For detailed expressions of the galaxy power spectrum that follows from the equations mentioned above, see Appendix A.

3.1.3 Redshift-space distortions

We base our description of the redshift-space power spectrum on (Scoccimarro, Couchman & Frieman 1999)

$$P(k,\mu) = \int \frac{{\rm d}^3r}{(2\pi)^3} {\rm e}^{-i\boldsymbol{k}\cdot\boldsymbol{r}}\, W(\lambda,\boldsymbol{r}) \Big[\langle {\rm e}^{\lambda\Delta u_z} D_s D_s' \rangle_c + \langle {\rm e}^{\lambda\Delta u_z} D_s \rangle_c + \langle {\rm e}^{\lambda\Delta u_z} D_s' \rangle_c \Big], \tag{15}$$

where $\lambda = ifk\mu$, $W(\lambda,\boldsymbol{r}) = \langle {\rm e}^{\lambda\Delta u_z}\rangle_c$ is the generating function of velocity differences, and $D_s \equiv \delta_g + f\nabla_z u_z$, with a prime denoting a quantity at $\boldsymbol{x}'$ instead of $\boldsymbol{x}$, and $\boldsymbol{r} = \boldsymbol{x} - \boldsymbol{x}'$. In the Gaussian approximation, the generating function can be written as

$$W_G(\lambda,\boldsymbol{r}) = {\rm e}^{\lambda^2(\sigma_v^2 - \psi_\perp + v^2\Delta\psi)}, \tag{16}$$

where $\psi_\perp = (I_0 + I_2)/3$, $\Delta\psi = I_2$, $\sigma_v^2 = \psi_\perp(0)$ and

$$I_\ell(r) \equiv \int {\rm d}^3k\; j_\ell(kr)\, \frac{P(k)}{k^2}. \tag{17}$$

In the large-scale limit $W_G(\lambda, \boldsymbol{r}\to\infty) = {\rm e}^{\lambda^2\sigma_v^2}$ becomes scale independent. However, as pointed out in Scoccimarro (2004), it is necessary to include non-linear corrections to this factor, which correspond mostly to fingers-of-God (FOG) or virial motions, since the large-scale limit of the velocity distribution function *is not* Gaussian. Therefore, instead of $W_G(\lambda,\boldsymbol{r}\to\infty)$ we use,

$$W_\infty(\lambda) = \frac{1}{\sqrt{1-\lambda^2 a_{\rm vir}^2}} \exp\left(\frac{\lambda^2\sigma_v^2}{1-\lambda^2 a_{\rm vir}^2}\right), \tag{18}$$

where $a_{\rm vir}$ is a free parameter that describes the contribution of small-scale velocities and characterizes the kurtosis of the velocity distribution, while σ_v is predicted as above. This is thus the form of our FOG factor, which can be obtained by resumming quadratic non-linearities as advocated in Scoccimarro (2004). To calculate the expression in square brackets (whose Fourier transform corresponds

roughly to a 'no-virial' power spectrum), we use the one-loop approximation:

$$P_{\rm novir}(k,\mu) = \int \frac{{\rm d}^3 r}{(2\pi)^3} {\rm e}^{-i\boldsymbol{k}\cdot\boldsymbol{r}} \Big[\langle D_s D_s' \rangle_c + \lambda \langle \Delta u_z D_s D_s' \rangle_c + \lambda^2 \langle \Delta u_z D_s \rangle_c \langle \Delta u_z D_s' \rangle_c \Big]. \quad (19)$$

Therefore, the result for the redshift-space power spectrum is given by

$$P(k,\mu) = W_\infty(ifk\mu)\, P_{\rm novir}(k,\mu), \quad (20)$$

and multipoles can be obtained directly by integrating this equation against Legendre polynomials $L_\ell(\mu)$ as in equation (7). We now briefly describe how we calculate each of the terms in equation (19). A more detailed description of the involved terms can be found in Appendix A.

The first term involving $\langle D_s D_s' \rangle_c$ is simply the non-linear version of the well-known Kaiser formula (Kaiser 1987),

$$P^{(1)}_{\rm novir}(k,\mu) = P_{gg}(k) + 2f\mu^2 P_{g\theta}(k) + f^2\mu^4 P_{\theta\theta}(k). \quad (21)$$

Assuming that there is no velocity bias, $P_{\theta\theta}(k)$ can be obtained directly from the predictions of gRPT. Appendix A contains explicit formulae for $P_{gg}(k)$ and $P_{g\theta}(k)$.

The term involving $\langle \Delta u_z D_s D_s' \rangle_c$ in equation (19) is to leading order given by the tree-level bispectrum between densities and velocities as

$$P^{(2)}_{\rm novir}(k,\mu) = \int \frac{q_z}{q^2} \Big[B_{\theta D_s D_s}(\boldsymbol{q}, \boldsymbol{k}-\boldsymbol{q}, -\boldsymbol{k}) + B_{\theta D_s D_s}(\boldsymbol{q}, -\boldsymbol{k}, \boldsymbol{k}-\boldsymbol{q}) \Big], \quad (22)$$

with the bispectra given by standard tree-level PT for densities and velocities in terms of the F_2 and G_2 kernels and bias parameters b_1, b_2, γ_2.

The term $\langle \Delta u_z D_s \rangle_c \langle \Delta u_z D_s' \rangle_c$ in equation (19) is already quadratic in the power spectrum, so this can be evaluated using linear perturbation theory. We then have

$$P^{(3)}_{\rm novir}(k,\mu) = \int \frac{q_z}{q^2} \frac{(k_z - q_z)}{(\boldsymbol{k}-\boldsymbol{q})^2} \left(b_1 + f\mu_q^2\right) \left(b_1 + f\mu_{k-q}^2\right) \times P_{\delta\theta}(k-q) P_{\delta\theta}(q) {\rm d}^3 q. \quad (23)$$

The closest redshift-space model in the literature to ours (Taruya et al. 2010; Beutler et al. 2014) also starts from equation (15). Our approach has three main differences, namely, we include non-linear bias contributions coming from b_2 and γ_2 to the bispectra in equation (22), our FOG factor equation (18) is non-Gaussian, we let γ_3^- be a free parameter (instead of being fixed to its local Lagrangian bias value), and we use gRPT to calculate matter loops instead of RegPT (which is not Galilean invariant). In summary, note that our redshift-space model has a single free parameter, $a_{\rm vir}$. It can be considered as the large-scale limit to a more complete model in which the velocity dispersion is considered to be scale dependent and other small-scale effects are taken into account (Scoccimarro, in preparation). The main reason for these simplifications is that the model as presented here can be numerically evaluated very efficiently for cosmological parameter estimation.

3.2 The Alcock–Paczynski effect

As described in Section 2, clustering measurements from real galaxy catalogues depend on the assumption of a fiducial cosmology used to transform the observed redshifts into comoving distances. Assuming a fiducial cosmology that deviates from the true underlying one leads to a rescaling of the components parallel and perpendicular to the line of sight, $s_\parallel$ and $s_\perp$, of the total separation vector $\mathbf{s}$ between two galaxies as (Padmanabhan & White 2008; Kazin et al. 2012)

$$s_\perp = q_\perp s_\perp', \quad (24)$$

$$s_\parallel = q_\parallel s_\parallel', \quad (25)$$

where the primes denote the quantities in the fiducial cosmology and the scaling factors are given by the ratios of the angular diameter distance and the Hubble parameter in the true and fiducial cosmologies at the mean redshift of the sample, $z_{\rm m}$, as

$$q_\perp = \frac{D_{\rm M}(z_{\rm m})}{D_{\rm M}'(z_{\rm m})}, \quad (26)$$

$$q_\parallel = \frac{H'(z_{\rm m})}{H(z_{\rm m})}. \quad (27)$$

Equations (24) and (25) are the basis of the AP test (Alcock & Paczynski 1979), which allows for anisotropic BAO measurements (Blake & Glazebrook 2003; Hu & Haiman 2003; Linder 2003). In terms of s and μ, these equations can be written as (Ballinger, Peacock & Heavens 1996)

$$s = s' q(\mu'), \quad (28)$$

$$\mu = \mu' \frac{q_\parallel}{q(\mu')}, \quad (29)$$

where

$$q(\mu) = \left[q_\parallel^2 (\mu')^2 + q_\perp^2 (1-(\mu')^2) \right]^{1/2}. \quad (30)$$

The scaling factors of equations (26) and (27) are often denoted $\alpha_{\perp,\parallel}$. However, we will reserve that notation for the combination of these purely geometric quantities with the sound horizon ratios in the fiducial and true cosmology, as described in Alam et al. (2016). For historical reasons, most clustering measurements are expressed in units of h^{-1} Mpc. As the value of h of a given cosmological model will in general be different from that of the fiducial cosmology, the ratios of equations (26) and (27) must also be computed in these units.

Before comparing the predictions of a given cosmological model with our BOSS clustering measurements, we use equations (28) and (29) to transform our model of $\xi(\mu, s)$ to the fiducial cosmology assumed in their estimation by expressing the integral in equation (1) as

$$\xi^{\prime\mu_2}_{\mu_1}(s') \equiv \frac{1}{\mu_2' - \mu_1'} \int_{\mu_1'}^{\mu_2'} \xi(\mu(\mu', s'), s(\mu', s'))\, {\rm d}\mu'. \quad (31)$$

3.3 Performance of the model

3.3.1 *Minerva simulations*

To evaluate the performance of the model described in Section 3.1, we used a set of 100 N-body simulations called MINERVA, which are described in more detail in Grieb et al. (2016a). These simulations represent different realizations of the same cosmology, corresponding to the best-fitting flat ΛCDM model to the combination of CMB data and the wedges of the CMASS sample from SDSS DR9 from Sánchez et al. (2013). This model is characterized by a matter density of $\Omega_{\rm m} = 0.285$, a baryon physical density of $\omega_{\rm b} = 0.022\,24$,

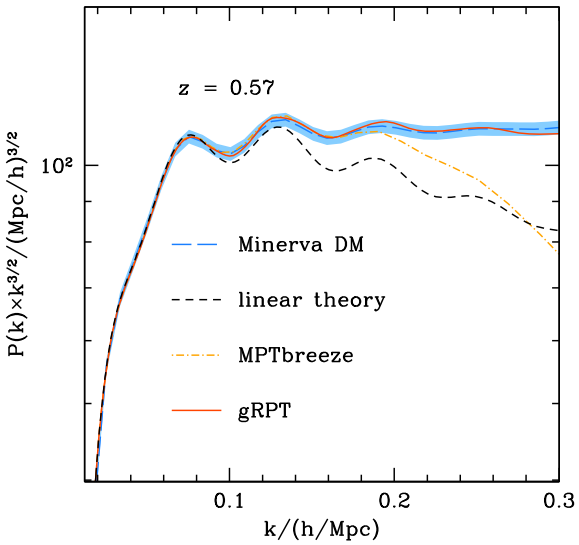

Figure 2. Mean dark matter real-space power spectrum of the MINERVA simulations at $z = 0.57$ (blue long-dashed lines) compared against the predictions of linear theory (black short-dashed lines), two-loop RPT as implemented in MPTBREEZE (orange dot–dashed lines) and one-loop gRPT (red solid lines). The shaded region corresponds to a 2 per cent uncertainty in the value of $P(k)$.

a Hubble constant of $H_0 = 69.5\,\mathrm{km\,s^{-1}\,Mpc^{-1}}$, a scalar spectral index of $n_s = 0.968$ and an amplitude of density fluctuations of $\sigma_8 = 0.828$. Each simulation traces the evolution of the dark matter density field with $N_{\mathrm{part}} = 1000^3$ over a box of side length $L_{\mathrm{box}} = 1.5\,\mathrm{Gpc}\,h^{-1}$. The initial conditions were generated with the second-order Lagrangian perturbation theory (2LPT) at a starting redshift of $z_{\mathrm{ini}} = 63$.

Fig. 2 shows a comparison of the mean dark matter real-space power spectrum of the MINERVA simulations at $z = 0.57$ with the predictions of RPT (dashed lines) computed using MPTBREEZE (Crocce, Scoccimarro & Bernardeau 2012), and one-loop gRPT (solid lines). The shaded regions correspond to a 2 per cent uncertainty in the value of $P(k)$. The prediction from RPT is in good agreement with the simulation results up to $k \lesssim 0.15\,h\,\mathrm{Mpc}^{-1}$ and describes accurately the damping of the first BAO peaks. Using gRPT, the description of the simulation results can be extended up to modes as high as $k \lesssim 0.25\,h\,\mathrm{Mpc}^{-1}$. As our model of the full shape of the clustering wedges is based on gRPT, we can expect to be able to extend the range of scales included in our analysis with respect to the analyses of Sánchez et al. (2013, 2014).

In order to extend these models to real galaxy clustering measurements, it is necessary to include the effects of bias and RSD. We model galaxy and halo bias including both local and non-local contributions given by the parameters b_1, b_2, γ_2 and γ_3^- defined in Section 3.1.2. As our two-point clustering measurements are not significantly sensitive to γ_2, we use the local Lagrangian relation of equation (13) to set its value in terms of b_1 and treat the remaining quantities as free parameters.

We used the snapshots at $z = 0.57$ of the MINERVA simulations, corresponding to the mean redshift of the CMASS sample, in which we identified bound haloes using a friends-of-friends algorithm. The resulting sample was later post-processed with SUBFIND (Springel et al. 2001) to eliminate spurious unbound objects, leading to a final halo catalogue with a minimum mass of $M_{\mathrm{min}} = 2.67 \times 10^{12}\,h^{-1}\,\mathrm{M}_\odot$. Grieb et al. (2016a) populated the Minerva halo catalogues at $z = 0.57$ with galaxies following a halo occupation distribution

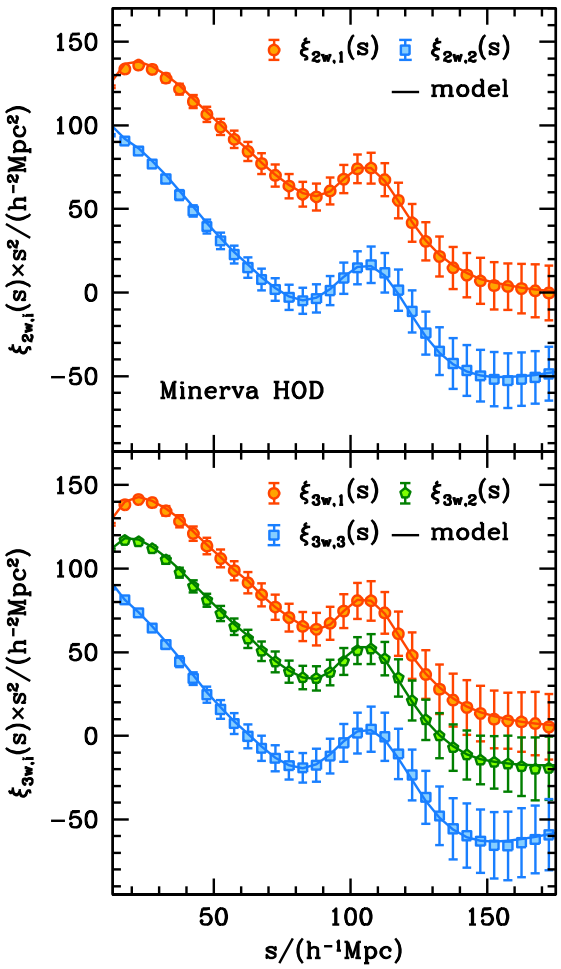

Figure 3. Mean clustering wedges of the MINERVA HOD samples for the two (upper panel) and three (lower panel) μ-bins configurations. The error bars correspond to the square root of the diagonal entries of the covariance matrices computed using the Gaussian recipes of Grieb et al. (2016a). The solid lines correspond to the model described in Section 3.1, which gives an excellent description of the simulation results.

(HOD) model parametrized as in Zheng, Coil & Zehavi (2007), in order to match the monopole correlation function of the CMASS sample. The values of the parameters characterizing this HOD are similar to those used by Manera et al. (2013), but the mass resolution of the MINERVA simulations allows us to resolve the haloes of the low-mass tail of the distribution. The clustering properties of the resulting HOD galaxy samples closely match those of the CMASS sample of BOSS. We use these HOD catalogues to test if our full model of equation (20) correctly describes the effect of non-linear evolution, bias and RSD, including the impact of the FOG effect, on a sample that contains both central and satellite galaxies.

The points in Fig. 3 correspond to the mean wedges from the HOD galaxies of all MINERVA realizations for two (upper panel) and three μ-bins (lower panel) configurations. As the 100 MINERVA realizations are not enough to obtain a robust estimate of the covariance matrix of these measurements, we use the Gaussian recipes of Grieb et al. (2016a), computed using the multipoles of the non-linear power spectrum model of Section 3.1 as input. The error bars in Fig. 3 correspond to the square root of the diagonal entries of the resulting covariance matrices. As shown by Grieb et al. (2016a), these Gaussian formulae give an excellent description of the

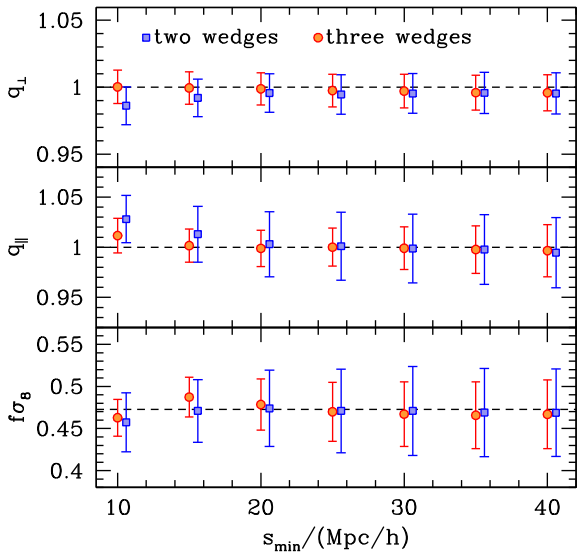

Figure 4. Mean values (points) and 68 per cent CL on $q_\perp$, $q_\parallel$ and $f\sigma_8$ derived from the measurements of two (squares) and three (circles) clustering wedges from the MINERVA HOD galaxy samples as a function of the minimum scale included in the fits. The dashed lines correspond to the true values of these parameters. Based on this test we set a minimum scale of $s_{\rm min} = 20\,h^{-1}$ Mpc for our fits to the BOSS combined sample clustering wedges.

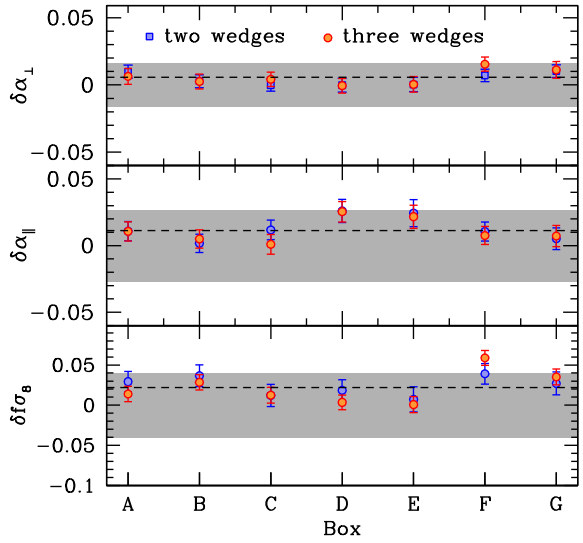

Figure 5. Difference between the values of $\alpha_\perp$, $\alpha_\parallel$ and $f\sigma_8$ obtained from the measurements of two (squares) and three (circles) wedges from each of the HOD boxes (labelled A–G) of the RSD challenge of Tinker et al. (in preparation). The dashed lines correspond to the mean differences over all boxes. The shaded regions indicate the uncertainties associated with the constraints on these parameters inferred from the real BOSS sample (see Section 5).

results inferred from the MINERVA simulations. Using these covariance matrices, we fitted for the nuisance parameters of the model using the measurements of two clustering wedges, while fixing all cosmological parameters to their true values. The solid lines in Fig. 3 correspond to the model described in Section 3.1, computed using the resulting values for the nuisance parameters, which show an excellent agreement with the results from the MINERVA simulations up to small scales.

In order to test the ability of our model to provide unbiased cosmological constraints, we treated the quantities $q_\perp$, $q_\parallel$ and $f\sigma_8$ as free parameters and fit for them using the mean clustering wedges from the MINERVA simulations, varying simultaneously the nuisance parameters of the model while fixing all cosmological parameters to their correct values (i.e. fixing the shape of the linear-theory power spectrum). Fig. 4 shows the obtained constraints for the cases of two (squares) and three (circles) wedges as a function of the minimum scale included in the fits, $s_{\rm min}$. The points indicate the mean values of these parameters derived from our Markov chain Monte Carlo (MCMC), while the error bars correspond to their respective 68 per cent confidence levels (CL). In all cases, the maximum scale was set to $s_{\rm max} = 160\,h^{-1}$ Mpc. The dashed lines in the same figure correspond to the true values of these parameters.

The constraints obtained using both configurations are in perfect agreement with the true underlying values of these parameters, but the 68 per cent CL obtained with three clustering wedges are significantly smaller than those recovered from the analysis of two μ-bins. This clearly illustrates the power of the additional information recovered from three clustering wedges, with respect to that of using only two. These results are consistent with those of the Fourier-space analysis of Grieb et al. (2016b), which is based on the same underlying model of non-linearities, bias and RSD. As $s_{\rm min}$ is reduced, the allowed ranges for all parameters decrease. The results from this test indicate that the application of the model described in Section 3.1 to a measurement of three clustering wedges can give unbiased cosmological constraints even when including scales as small as $s_{\rm min} \simeq 15\,h^{-1}$ Mpc. As this limit might depend on the details of the cosmological model, we fixed the value of $s_{\rm min} = 20\,h^{-1}$ Mpc for our analysis of the clustering wedges from the BOSS combined galaxy sample.

3.3.2 *The BOSS RSD challenge*

Our companion paper Tinker et al. (in preparation) presents the results of a comparison or 'challenge' of various RSD models and methodologies to extract cosmological information from the full shape of anisotropic clustering measurements. This challenge consisted of two different tests: an ensemble of 83 mock catalogues of the NGC CMASS subsample, and a series of seven simulation boxes corresponding to different cosmologies and HOD parametrizations. A more detailed description of these data sets and the results obtained by the different methods can be found in Tinker et al. (in preparation). Here, we summarize the results obtained by applying the model described in Section 3.1 to the measurements of three clustering wedges in configuration space obtained from these data sets.

Fig. 5 shows the difference between the values of $\alpha_\perp$, $\alpha_\parallel$ and $f\sigma_8$ recovered from the measurements of $\xi_{\rm 3w}(s)$ from each of the seven HOD boxes, labelled A–G [see Tinker et al. (in preparation) for details on the HOD applied in each case]. The dashed lines correspond to the mean differences over all boxes. A covariance matrix derived from a set of 1000 QPMs (White et al. 2014) simulations with a box size of $2.5\,h^{-1}$ Gpc and an HOD matching the clustering of the CMASS sample was used for all the fits. As these results correspond to different cosmologies and HODs, it is not possible to derive a general conclusion about the expected deviation between the true and obtained results. However, with the exception of the value of $f\sigma_8$ recovered from box F, the obtained deviations are always smaller than the uncertainties with which these parameters can be recovered from the BOSS sample (see Section 5), which are indicated by the grey shaded regions. More details can be found

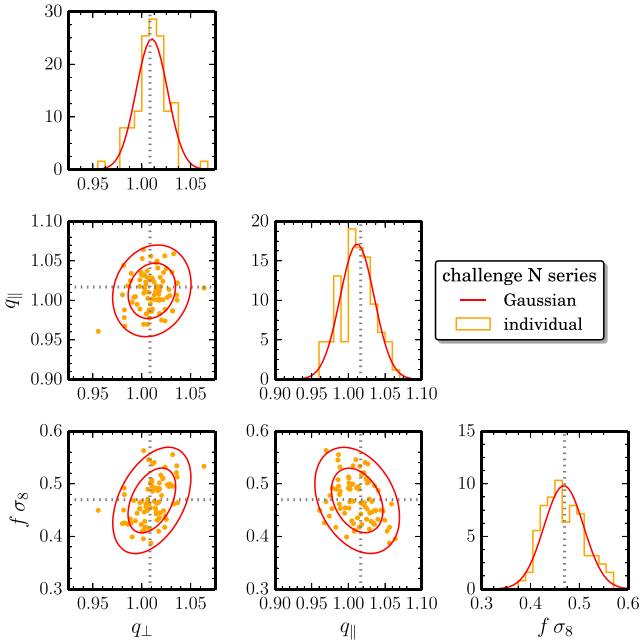

Figure 6. Constraints on $q_\perp$, $q_\parallel$ and $f\sigma_8$ obtained from the 83 CMASS mock catalogues of the RSD challenge of Tinker et al. (in preparation.). The points in the off-diagonal panels correspond to the values recovered from the individual mocks, while the histograms in the diagonal panels show the distribution of the obtained results from the full set of mocks. The red solid lines correspond to a Gaussian fit to the obtained distribution.

in Tinker et al. (in preparation), but the HOD of box F includes the effect of assembly bias weighted to high densities. Other methods based on configuration-space measurements give similar results when applied to box F. At least part of the observed deviations could be due to cosmic variance, but this result could signal the limitations of these methods to deal with assembly bias (which is not explicitly taken into account in our model). However, as this result is based on a single box, we leave a more detailed study of the possible impact of assembly bias on the obtained constraints for a future analysis.

Fig. 6 summarizes the constraints on $q_\perp$, $q_\parallel$ and $f\sigma_8$ obtained from the set of 83 CMASS mock catalogues. The points in the off-diagonal panels correspond to the recovered values of these parameters from each individual realizations, while the histograms in the diagonal panels show the distribution of the obtained results from the full set of mocks. The red solid lines correspond to the Gaussian fit to the obtained distribution. The constraints obtained using our methodology are in excellent agreement with the true underlying values of these parameters indicated by the dotted lines.

3.3.3 *The MD-PATCHY mock catalogues*

As a final test of our model, we applied to the measurements of $\xi_{3w}(s)$ from each of the 2045 MD-PATCHY mocks of the BOSS DR12 combined sample described in Section 2.2. Besides providing another test for possible systematic errors in our constraints, the obtained values can give us an idea of the uncertainties we can expect to obtain from the analysis of the real BOSS data. These constraints are also used in Sánchez et al. (2016) to compute the cross-correlation coefficients between the results inferred from $\xi_{3w}(s)$ and those of our companion papers.

Table 1 lists the mean and dispersion of the difference between values of $\alpha_\perp$, $\alpha_\parallel$ and $f\sigma_8$ obtained from the MD-PATCHY mocks and their correct values in each of our three redshift bins. Deviations of the order of 0.3σ and 0.2σ can be seen in the value of $f\sigma_8$ obtained using data from the low- and intermediate-redshift bins, respectively. Although this might indicate the presence of a small systematic error in these measurements, as these differences are much smaller than their associated statistical errors we do not include a systematic uncertainty in our results.

Table 1. Mean and dispersion of the deviations between the parameter constraints obtained from the individual MD-PATCHY mock catalogues and their true underlying values for our three redshift bins.

Parameter	$0.2 < z < 0.5$	$0.4 < z < 0.6$	$0.5 < z < 0.75$
$\delta\alpha_\perp$	0.003 ± 0.022	0.001 ± 0.018	0.001 ± 0.018
$\delta\alpha_\parallel$	0.006 ± 0.032	0.005 ± 0.027	0.005 ± 0.028
$\delta f\sigma_8$	-0.018 ± 0.052	0.009 ± 0.044	0.004 ± 0.044

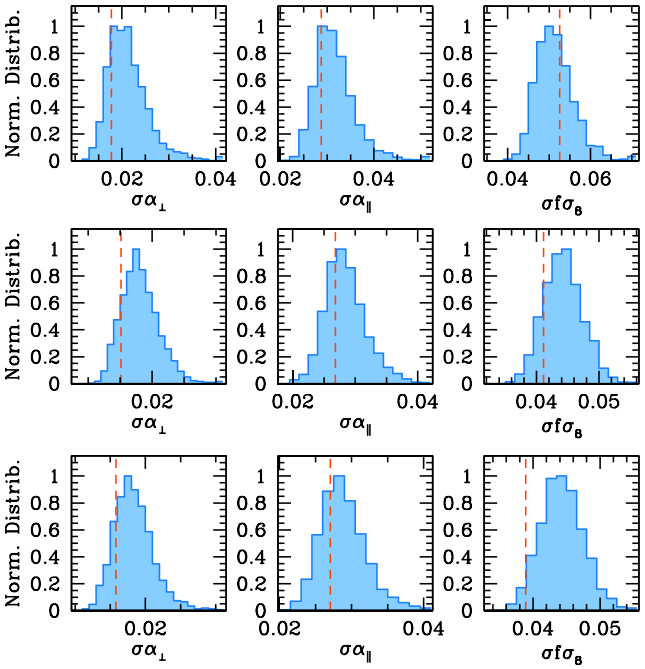

Figure 7. Distributions of the marginalized 68 per cent CL on the values of the parameters $\alpha_\perp$, $\alpha_\parallel$ and $f\sigma_8$ obtained from the individual MD-PATCHY mocks in each of our three redshift bins. The vertical dashed lines indicate uncertainties on these parameters obtained from the real BOSS clustering wedges (see Section 5).

Fig. 7 shows the distributions of the marginalized 68 per cent CL on the values of $\alpha_\perp$, $\alpha_\parallel$ and $f\sigma_8$ obtained from the PATCHY mocks in the low- (upper panels), intermediate- (middle panels) and high-redshift (lower panels) bins. The vertical dashed lines indicate the uncertainties on these parameters obtained from the real BOSS clustering wedges as described in Section 5, which are in good agreement with the distributions obtained from the MD-PATCHY mocks.

4 COSMOLOGICAL IMPLICATIONS

4.1 Methodology for parameter constraints

We derive cosmological constraints from our BOSS clustering measurements following the same methodology as in Sánchez et al. (2014), with small modifications. The clustering wedges of the

Table 2. Cosmological parameters constrained in our analysis. The upper part lists the parameters of the standard ΛCDM model while the middle section lists a number of its possible extensions. The lower part lists a number of additional quantities whose values can be derived from the first two sets.

Parameter	Description
Parameters of the standard ΛCDM model	
$\theta_{\rm MC}$	Approximate angular size of the sound horizon at recombination[a]
$\omega_{\rm b}$	Physical baryon density
$\omega_{\rm c}$	Physical cold dark matter density
τ	Optical depth to reionization
$n_{\rm s}$	Scalar spectral index[b]
$A_{\rm s}$	Amplitude of the scalar perturbations[b]
Extensions to the standard model	
w_0	Present-day dark energy equation of state, $w_{\rm DE}$
w_a	Time-dependence of $w_{\rm DE}$ (assuming $w_{\rm DE}(a) = w_0 + w_a(1-a)$)
Ω_k	Curvature contribution to energy density
$\sum m_\nu$	Total sum of the neutrino masses
γ	Power-law index of the structure growth rate parameter, assuming $f(z) = \Omega_{\rm m}^{\gamma}$
Derived parameters	
$\Omega_{\rm m}$	Total matter density
$\Omega_{\rm DE}$	Dark energy density
h	Dimensionless Hubble parameter
σ_8	Linear-theory rms mass fluctuations in spheres of radius $8\,h^{-1}$ Mpc
S_8	$\sigma_8\sqrt{\Omega_{\rm m}/0.3}$

Notes. [a]Defined as in the 2015 July version of COSMOMC.
[b]Quoted at the pivot wavenumber of $k_0 = 0.05\,h\,{\rm Mpc}^{-1}$.

Table 3. The marginalized 68 per cent constraints on the most relevant cosmological parameters of the extensions of the ΛCDM model analysed in Sections 4.3–4.6, obtained using different combinations of the data sets described in Section 4.1. Appendix B contains a complete list of the constraints obtained in each case.

	Planck+BOSS	Planck+BOSS +SN
Constant dark energy equation of state		
$w_{\rm DE}$	$-0.991^{+0.062}_{-0.047}$	-0.996 ± 0.042
$\Omega_{\rm m}$	$0.308^{+0.014}_{-0.012}$	0.306 ± 0.011
Time-dependent dark energy equation of state		
w_0	$-0.73^{+0.27}_{-0.18}$	-0.92 ± 0.10
w_a	$-0.83^{+0.58}_{-0.80}$	$-0.32^{+0.45}_{-0.36}$
$\Omega_{\rm m}$	0.325 ± 0.020	0.308 ± 0.010
Non-flat models		
$100\Omega_k$	$-0.01^{+0.34}_{-0.31}$	-0.07 ± 0.30
$\Omega_{\rm DE}$	0.715 ± 0.0145	0.6941 ± 0.0079
$\Omega_{\rm m}$	0.288 ± 0.016	$0.3052^{+0.0079}_{-0.0095}$
Dark energy and curvature		
$w_{\rm DE}$	$-0.977^{+0.076}_{-0.070}$	$-0.985^{+0.053}_{-0.049}$
$100\Omega_k$	$0.16^{+0.38}_{-0.43}$	$0.10^{+0.36}_{-0.39}$
$\Omega_{\rm m}$	0.308 ± 0.13	0.306 ± 0.010
Massive neutrinos		
$\sum m_\nu$/(eV)	<0.26 (95 per cent CL)	<0.25 (95 per cent CL)
$\Omega_{\rm m}$	$0.310^{+0.009}_{-0.013}$	$0.308^{+0.009}_{-0.011}$
Deviations from GR		
γ	0.609 ± 0.079	$<0.610 \pm 0.079$ (95 per cent CL)
$\Omega_{\rm m}$	$0.3049^{+0.0078}_{-0.0092}$	$0.3042^{+0.0074}_{-0.0087}$
Dark energy and modified gravity		
γ	$0.65^{+0.10}_{-0.13}$	$0.627^{+0.086}_{-0.099}$
$w_{\rm DE}$	$-1.05^{+0.10}_{-0.08}$	$-1.016^{+0.053}_{-0.046}$

overlapping redshift bin are strongly covariant with those obtained in the two independent bins and do not lead to a significant improvement in the total constraining power of our measurements. Therefore, to avoid the complication of including the covariance between our clustering measurements in this section, we use only the information from the wedges measured in our low- and high-redshift bins, and refer to these data sets as 'BOSS $\xi_{\rm 3w}$'. We use our BOSS $\xi_{\rm 3w}$ data set in combination with the latest CMB temperature and polarization power spectra from the *Planck* satellite (Planck Collaboration XIII 2016), to which we refer simply as 'Planck'. We do not include CMB lensing information. We also use the information from the joint SDSS-II and Supernova Legacy Survey Light-Curve Analysis Type Ia supernovae (SN) sample (JLA; Betoule et al. 2014).

We use the 2015 July version of COSMOMC (Lewis & Bridle 2002), which in turn uses CAMB to compute the linear-theory CMB and matter power spectra (Lewis, Challinor & Lasenby 2000), modified to compute the model of non-linearities, bias and RSD described in Section 3.1. We constrain the cosmological parameters listed in Table 2 by directly comparing the theoretical predictions obtained for a given model with the galaxy clustering measurements themselves. Note that this approach is different from the one followed in Alam et al. (2016), where the combined growth and geometric constraints of the various BOSS clustering analyses (including those derived in Section 5) are used as a proxy for these measurements and compared with the predictions from different cosmological models. In Section 4.2, we explore the parameter space of the standard flat ΛCDM model, where the dark energy component is characterized by an equation-of-state parameter $w_{\rm DE} = p_{\rm DE}/\rho_{\rm DE} = -1$, by varying the six parameters of the upper section of Table 2. In Sections 4.3–4.6, we constrain a number of possible extensions of the ΛCDM model by allowing for variations on the parameters presented in the middle section of Table 2. We consider more general dark energy models, non-zero curvature, varying contributions from massive neutrinos, and possible deviations from GR. Table 3 summarizes the constraints on these cosmological parameters obtained from the combination of the Planck CMB measurements with the full shape of the clustering wedges from BOSS, and when this information is combined with the JLA SN data. When it is not treated as a free parameter, we assume a non-zero massive neutrino component with a total mass $\sum m_\nu = 0.06$ eV. For all parameter spaces, we also follow the constraints on the derived quantities listed on the final part of Table 2. In all cases, the nuisance parameters of the model, b_1, b_2, γ_3^- and $a_{\rm vir}$, are also included in our MCMC and marginalized over.

Grieb et al. (2016b) perform an analysis of the cosmological implications of the BOSS DR12 combined sample similar to the one presented here but based on Fourier-space clustering measurements, which are combined with the same CMB and SN data sets used here (see their section 5). They use the full shape of the Fourier-space wedges obtained by filtering out the information of Legendre multipoles $\ell > 4$, which are fitted with theoretical predictions based on

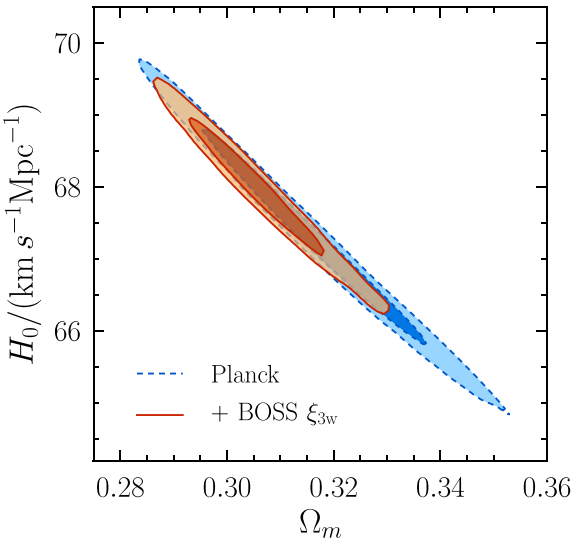

Figure 8. The marginalized posterior distribution in the Ω_m–h plane for the ΛCDM parameter set. The dashed lines show the 68 and 95 per cent contours obtained using the CMB measurements from Planck alone. The solid contours correspond to the results obtained from the combination of the Planck data plus the full shape of the BOSS DR12 combined sample clustering wedges $\xi_{3w}(s)$.

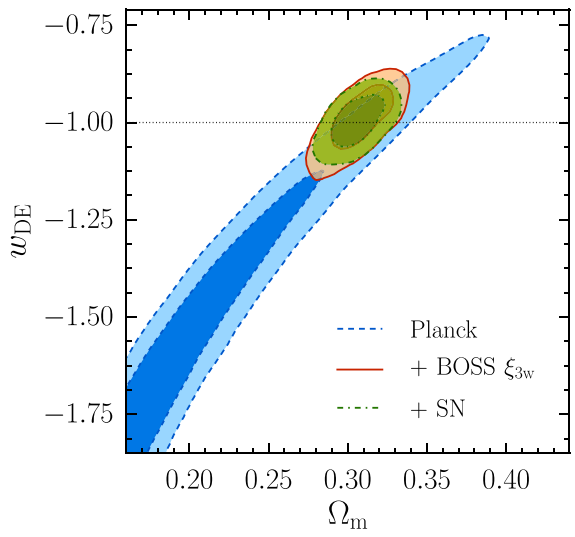

Figure 9. The marginalized posterior distribution in the Ω_m–w_{DE} plane for the ΛCDM parameter set extended by treating the redshift-independent value of w_{DE} as a free parameter. The dashed lines show the 68 and 95 per cent contours obtained using Planck CMB data alone. The solid contours correspond to the results inferred from the combination of Planck and our BOSS $\xi_{3w}(s)$ measurements. The dot–dashed lines indicate the results obtained when the JLA SN sample is also included in the analysis. The dotted line indicates the standard ΛCDM value of $w_{DE} = -1$.

the model of non-linearities, bias and RSD described in Section 3. Thus, our analyses represent the first time that the same model is applied in configuration and Fourier-space fits. A comparison of the results of Grieb et al. (2016b) with those presented here shows excellent agreement, with both sets of measurements providing similar constraining power.

4.2 The ΛCDM parameter space

In this section, we focus on the constraints on the parameters of the standard ΛCDM model. The dashed lines in Fig. 8 show the two-dimensional marginalized constraints in the Ω_m–h plane obtained using Planck data alone. As described in (Percival et al. 2002), CMB-only results follow a narrow degeneracy that can be well described by a constant value of $\Omega_m h^3$. The solid lines in Fig. 8 show the result of combining the Planck data set with the configuration-space clustering wedges of BOSS. The information provided by our measurements of $\xi_{3w}(s)$ at low redshift leads to a significant improvement of the obtained constraints, with $\Omega_m = 0.3054 \pm 0.0087$ and $h = 0.6798 \pm 0.0065$. These results represent constraints at the 2.8 and 1 per cent level and are essentially unchanged by the inclusion of the information from SN measurements. The fact that these data sets can constrain the basic parameters of the ΛCDM model to this precision is a clear illustration of the constraining power achieved by current CMB and LSS measurements. Appendix B gives a summary of the constraints on the full set of cosmological parameters of the ΛCDM model.

The best-fitting ΛCDM model gives a good description of our measurements of the clustering wedges, with χ^2 values of 90 and 82 for the low- and high-redshift bins, respectively, for 84 bins. This model is also very close to the parameters values that best describe the Planck CMB data alone, showing the consistency between these data sets.

4.3 The dark energy equation of state

In the ΛCDM model, the dark energy component can be described as vacuum energy, which behaves analogously to a cosmological constant. In this section, we explore the constraints on more general dark energy models. We start by treating the redshift-independent value of w_{DE} as an additional parameter. The dashed lines in Fig. 9 correspond to the two-dimensional marginalized constraints in the Ω_m–w_{DE} plane obtained from the Planck CMB measurements, which follow a degeneracy that spans a wide range of values of these parameters. The solid lines in the same figure correspond to the constraints obtained when the Planck data are combined with our BOSS $\xi_{3w}(s)$ data set. The information encoded in these measurements provides much tighter constraints than in the previous case, leading to $\Omega_m = 0.308^{+0.014}_{-0.012}$ and $w_{DE} = -0.991^{+0.062}_{-0.047}$. This result is in excellent agreement with the standard ΛCDM model value of $w_{DE} = -1$, indicated by a dotted line in Fig. 9. The dot–dashed contours correspond to the results obtained by including also the information from the JLA SN data, leading to our final constraints of $\Omega_m = 0.306 \pm 0.011$ and $w_{DE} = -0.996 \pm 0.042$.

In more general dark energy models, the equation-of-state parameter might be a function of time. To explore this possibility, we use the linear parametrization of Chevallier & Polarski (2001) and Linder (2003) given by

$$w_{DE}(a) = w_0 + w_a(1 - a), \tag{32}$$

where a is the scalefactor and w_0 and w_a are free parameters. The dashed lines in Fig. 10 show the marginalized constraints in the w_0–w_a plane obtained using Planck data alone, which cover a large fraction of the parameter space. The solid lines show the effect of including the information from the BOSS $\xi_{3w}(s)$ measurements in the analysis. Although the LSS information leads to a significant reduction of the allowed region for these parameters, the resulting constraints on w_0 and w_a exhibit a strong degeneracy that allows for models whose behaviour can be significantly different to

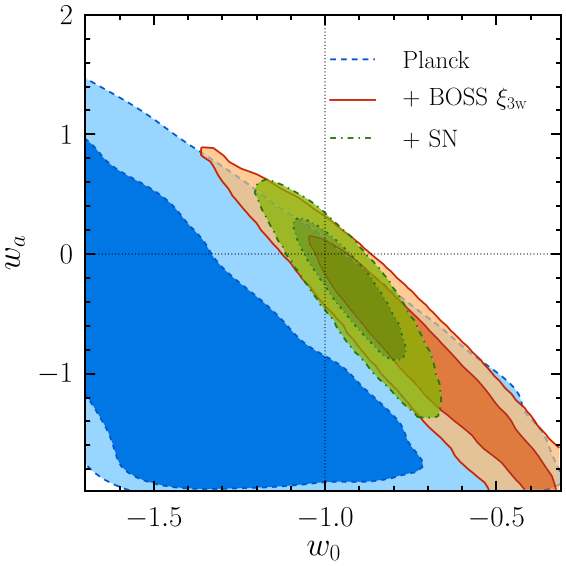

Figure 10. Marginalized 68 and 95 per cent CL in the w_0–w_a plane, the parameters controlling the redshift evolution of the dark energy equation of state, parametrized as in equation (32). The contours show the results obtained using the Planck CMB data alone (dashed lines), the combination of Planck and the BOSS $\xi_{3w}(s)$ (solid lines), and when this information is combined with the JLA SN data set (dot–dashed lines). The fiducial values of these parameters in the ΛCDM model are indicated by the dotted lines.

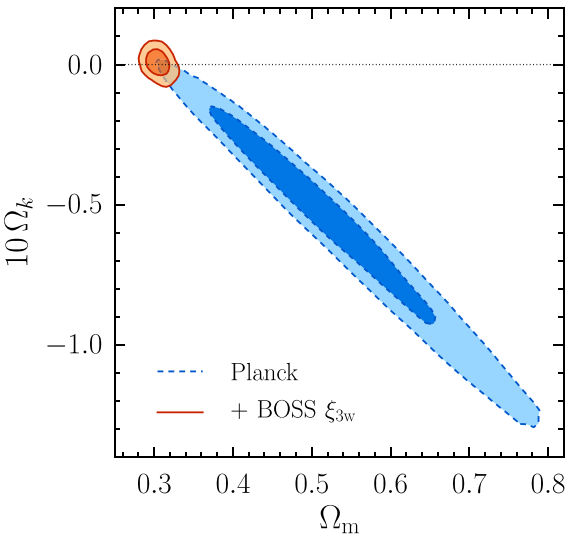

Figure 11. The marginalized posterior distribution in the Ω_m–Ω_k plane for the ΛCDM parameter set extended to allow for non-flat models. The contours show the 68 and 95 per cent contours obtained using Planck information alone (dashed lines) and the combination of these CMB data plus the clustering wedges of the final BOSS. The dotted line corresponds to the ΛCDM model, where $\Omega_k = 0$.

a cosmological constant. Additionally, including information from the JLA SN sample helps us to reduce the allowed region of the parameter space even further, leading to our final constraints of $w_0 = -0.92 \pm 0.10$ and $w_a = -0.32^{+0.45}_{-0.36}$, in good agreement with the ΛCDM values indicated by the dotted lines in Fig. 10.

4.4 The curvature of the universe

In this section, we focus on non-flat models and extend the ΛCDM parameter space to models with $\Omega_k \neq 0$. The dashed lines in Fig. 11 show the constraints in the Ω_m–Ω_k plane obtained by the Planck CMB measurements alone, which allow for significant deviations from a flat universe due to the well-known geometric degeneracy (Efstathiou & Bond 1999). The information from the clustering wedges from BOSS efficiently breaks this degeneracy, reducing the allowed region of the parameter space to a small area centred on the flat Universe value $\Omega_k = 0$, which is shown by the dotted line. As indicated in Table 3, these data sets can constrain the curvature of the Universe to $\Omega_k = -0.0001^{+0.0034}_{-0.0030}$. Additionally, including the JLA SN does not significantly improve the results over those obtained using the Planck+BOSS ξ_{3w} combination, with a final constraint of $\Omega_k = -0.0007 \pm 0.0030$ obtained from the combination of all data sets.

When Ω_k and w_{DE} are varied simultaneously, the geometric degeneracy extends to a two-dimensional sheet in the parameter space, degrading even more the constraints obtained from CMB information alone. This is shown by in the dashed contours in Fig. 12, which correspond to the 68 and 95 per cent CL in the w_{DE}–Ω_k plane derived from the Planck CMB measurements. The information in the full shape of the wedges $\xi_{3w}(s)$ is still very effective at reducing the allowed region for these parameters, which shrinks to a small area around the standard ΛCDM values indicated by the dotted lines. In this case, we find $\Omega_k = 0.0016^{+0.0038}_{-0.0043}$ and $w_{DE} = -0.977^{+0.076}_{-0.070}$. As shown by the dot–dashed lines in Fig. 12, these constraints

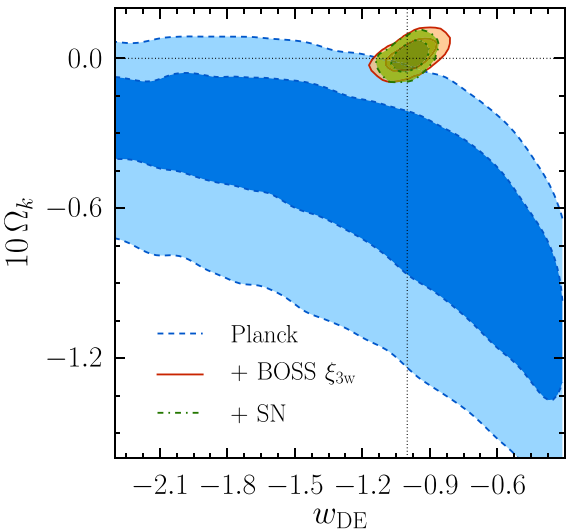

Figure 12. The marginalized constraints in the w_{DE}–Ω_k plane for the ΛCDM parameter set extended by allowing for simultaneous variations on both of these parameters. The contours correspond to the 68 and 95 per cent CL derived from the Planck CMB data alone (dashed lines), the combination of Planck plus the clustering wedges (solid lines), and when the JLA SN data sets are added to the later combination (dot–dashed lines). The dotted lines correspond to the values of these parameters in the ΛCDM model.

are slightly improved when the JLA SN information is also included in the analysis. In this case, we find $\Omega_k = 0.0010^{+0.0036}_{-0.0039}$ and $w_{DE} = -0.985^{+0.053}_{-0.048}$. These constraints are similar to the ones we find when only one of these parameters is allowed to deviate from their standard values. This indicates that current constraints on the dark energy equation of state do not depend strongly on the assumption of a flat Universe.

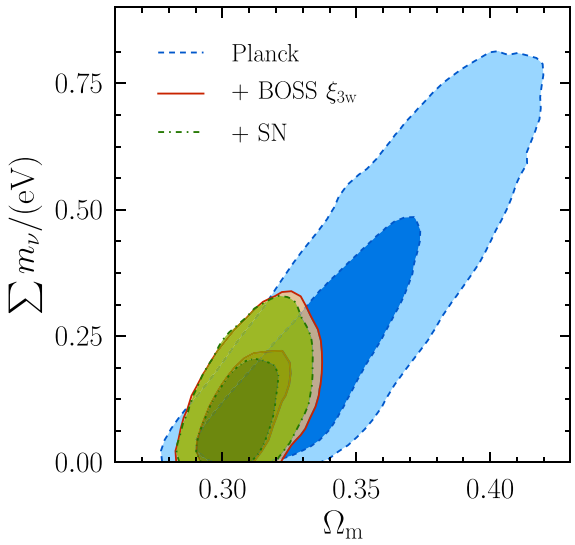

Figure 13. The marginalized posterior distribution in the Ω_m–Σm_ν plane for the ΛCDM parameter set extended by allowing for massive neutrinos. The dashed and solid lines correspond to the 68 and 95 per cent CL derived from the Planck CMB measurements alone (dashed lines) and by combining them with the BOSS $\xi_{3w}(s)$ measurements (solid lines).

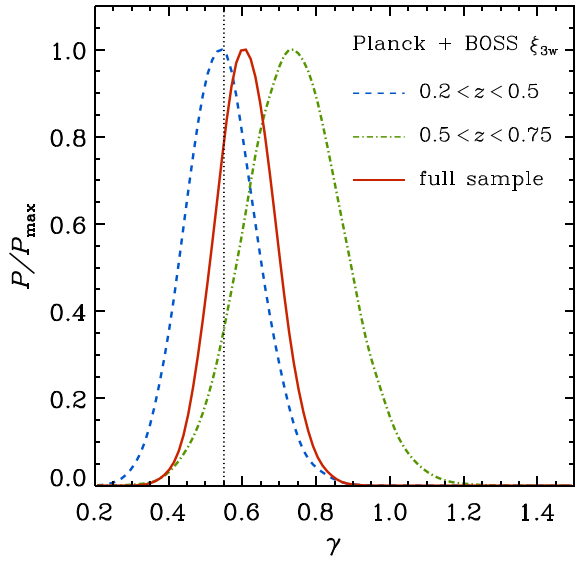

Figure 14. The one-dimensional marginalized posterior distribution of the power-law index of the structure growth-rate parameter γ derived from the combination of the CMB measurements from Planck and the BOSS $\xi_{3w}(s)$ (solid lines). These results are consistent with the value of $\gamma = 0.55$ predicted by GR, which is indicated by the dotted line. The dashed and dot–dashed lines correspond to the results obtained when the CMB data are separately combined with the clustering wedges of our low- and high-redshift bins, respectively.

4.5 Massive neutrinos

The combination of CMB and galaxy clustering measurements offers one of the best observational windows into neutrino masses. In the previous sections, we assumed a total neutrino mass of $\sum m_\nu = 0.06$ eV, the minimum value allowed by neutrino oscillation experiments under the assumption of a normal hierarchy (Otten & Weinheimer 2008). We now explore the constraints obtained when the total neutrino mass is allowed to vary freely. Fig. 13 shows the 68 and 95 per cent constraints in the Ω_m–$\sum m_\nu$ plane obtained when the ΛCDM parameter space is extended by treating $\sum m_\nu$ as a free parameter. The dashed lines correspond to the results obtained using the Planck CMB data alone. A higher total neutrino mass leads to an increase in the redshift of matter-radiation equality, which can be compensated by an increase in Ω_m in order to leave the CMB power spectrum unaffected. This is the origin of the degeneracy followed by the CMB-only constraints. Including the low-redshift information from the BOSS clustering wedges helps us to break this degeneracy, significantly improving the constraints. In this case, we find a limit of $\sum m_\nu < 0.25$ eV at the 95 per cent CL, which is almost unchanged by additionally including the JLA SN data.

4.6 Consistency with GR

In the context of GR, the redshift evolution of the structure growth-rate parameter can be accurately computed as

$$f(z) = \Omega_\mathrm{m}(z)^\gamma, \tag{33}$$

with $\gamma = 0.55$ with a small correction depending on the value of w_DE (Linder & Cahn 2007). This means that measurements of $f(z)$ as those obtained from anisotropic clustering measurements can be used as a test of the predictions of GR. This information is essential to distinguish between the dark energy and modified gravity scenarios for the origin of the current phase of accelerated expansion of the Universe (Zhang et al. 2007; Guzzo et al. 2008). The measurements of $f(z)$ obtained from anisotropic clustering measurements could be directly compared with the predictions of specific modified gravity models (e.g. Raccanelli et al. 2013; Wyman, Jennings & Lima 2013; Taruya et al. 2014; Song et al. 2015; Barreira, Sánchez & Schmidt 2016). Here, we follow a simpler approach and treat γ in equation (33) as a free parameter. In this way, the information on the growth of the structure contained in our galaxy clustering measurements can be used as a consistency test of GR. Assuming $w_\mathrm{DE} = -1$, a detection of a deviation from $\gamma = 0.55$ can be interpreted as an indication that the growth of density fluctuations is not consistent with the predictions of GR.

We tested the consistency of our clustering measurements with GR by extending the ΛCDM parameter space using equation (33) to compute $f(z)$ and treating γ as a free parameter. The solid line in Fig. 14 corresponds to the one-dimensional marginalized constraints on γ obtained from the combination of the Planck CMB measurements with the full shape of the BOSS $\xi_{3w}(s)$ clustering wedges. In this case, we find $\gamma = 0.609 \pm 0.079$, in good agreement with the GR prediction of $\gamma = 0.55$ indicated by the vertical dotted line. Additionally, including the JLA SN data does not improve this result. The dashed and dot–dashed lines correspond to the results obtained when the Planck CMB data are separately combined with the information from the wedges measured in our low- and high-redshift bins, respectively. While the constraint of $\gamma = 0.543 \pm 0.096$ obtained in the former case is in excellent agreement with GR, the latter case prefers a higher value, with $\gamma = 0.74 \pm 0.13$.

If the growth of structure is assumed to follow the predictions of GR of equation (33) with $\gamma = 0.55$, the measurements of the redshift evolution of $f(z)$ obtained from RSD can be translated into constraints on the matter density parameter. When this assumption is relaxed by allowing γ to vary freely this information is lost, leading to weaker constraints on w_DE (Amendola, Quercellini & Giallongo 2005). To test this, we extended the ΛCDM parameter space by allowing for simultaneous variations of w_DE (assumed

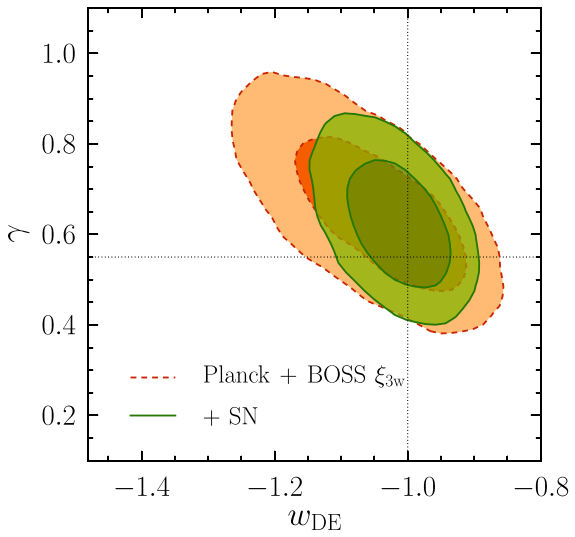

Figure 15. The marginalized posterior distribution in the w_{DE}–γ plane for the ΛCDM parameter set extended by allowing for simultaneous variations on both of these parameters. The contours correspond to the 68 and 95 per cent CL derived from the combination of the Planck CMB measurements plus the clustering wedges (solid lines), and when the JLA SN data set is also added to the analysis (dot–dashed lines). The dotted lines correspond to the values of these parameters in the standard ΛCDM + GR model.

time independent) and γ. Fig. 15 presents the two-dimensional marginalized constraints in the γ–w_{DE} plane obtained by means of the Planck+BOSS ξ_{3w} combination (dashed lines), and when these data are combined with the JLA SN sample (solid lines). Including γ as a free parameter degrades the constraints on the dark energy equation of state with respect to the results of Section 4.3. In this case, we find $w_{DE} = -1.05^{+0.10}_{-0.08}$ and $\gamma = 0.65^{+0.10}_{-0.13}$. Including the JLA SN data reduces the allowed region for these parameters, leading to $w_{DE} = -1.016^{+0.053}_{-0.046}$ and $\gamma = 0.627^{+0.086}_{-0.099}$, similar to the ones derived when these parameters are varied separately and are in agreement with the standard ΛCDM+GR cosmological model.

5 BAO AND RSD CONSTRAINTS

In most anisotropic clustering analyses, the cosmological information contained in the full shape of the clustering measurements is compressed into constraints on the parameter combinations $D_M(z)/r_d$, $H(z)r_d$ and $f\sigma_8(z)$ and their respective covariance matrix. Alternatively, these constraints are often expressed in terms of the analogous combinations $D_V(z)/r_d$, where

$$D_V(z) = \left(D_M(z)^2 \frac{cz}{H(z)} \right)^{1/3}, \tag{34}$$

and the AP parameter

$$F_{AP}(z) = D_M(z)H(z)/c. \tag{35}$$

This information is then used as a proxy for the LSS measurements when deriving constraints on cosmological parameters. Here, we use the model described in Section 3.1 to derive constraints on these parameters from the clustering wedges ξ_{3w} of the final BOSS combined galaxy sample in each of our three redshift bins. To this end, we fixed the values of ω_b, ω_c and n_s to match the best-fitting ΛCDM model to the CMB measurements from Planck (fixing in this way the shape of the linear-theory power spectrum) and treated the values of $\alpha_\perp$, $\alpha_\parallel$ and $f\sigma_8$ as free parameters using separately the clustering wedges of each redshift bin. The nuisance parameters of the model, b_1, b_2, γ_3^- and a_{vir}, are also included in our MCMC and marginalized over. This reproduces the analysis of the PATCHY mock catalogues described in Section 3.3.3 on the real clustering measurements from BOSS. The lines in Fig. 1 correspond to the best-fitting models obtained in this way for each of our redshift bins, which are characterized by reduced χ^2 values of 1.15, 1.07 and 1.03 for our low-, intermediate- and high-redshift bins, respectively.

The solid lines in Fig. 16 show the two-dimensional marginalized posterior distributions of $D_V(z)/r_d$, $F_{AP}(z)$ and $f\sigma_8(z)$ for each of our three redshift bins. The dotted lines in the same figure correspond to the Gaussian approximation of these constraints, which give a good description of the full distributions. The corresponding mean values and their covariance matrices are listed in Tables 4 and 5, respectively. The dashed lines in Fig. 16 correspond to the constraints inferred from the Planck CMB measurements under the assumption of a ΛCDM model. The agreement between these results and the ones obtained from the BOSS clustering wedges indicates the consistency between these data sets and their agreement with the ΛCDM model.

As shown in Alam et al. (2016), a comparison of our results with those of our companion papers shows good agreement. At all redshifts, the constraints derived from the wedges analyses presented here and in Grieb et al. (2016b) are tighter than the ones of the multipole analyses. Rather than the statistics used in the analysis, this is due to the fact that the model described in Section 3 makes it possible to use the information from smaller scales, where the effects of non-linearities and RSD are stronger. Alam et al. (2016) combine the results from the different BOSS analyses into a final set of consensus constraints using the methodology described in Sánchez et al. (2016). These consensus results are slightly tighter than those of the individual analyses showing that additional information is gained from the combination.

6 CONCLUSIONS

We have analysed the cosmological implications of the measurements of three clustering wedges $\xi_{3w}(s)$ of the final galaxy samples from BOSS corresponding to SDSS-DR12. We make use of the BOSS combined sample described in Reid et al. (2016), containing the joint information of the LOWZ and CMASS samples that were analysed separately in former studies, including also the early regions that were previously excluded.

We have focused on adjusting our analysis methodology to maximize the information extracted from the BOSS data. We implemented a state-of-the-art description of the effects of the non-linear evolution of density fluctuations, bias and RSD that allowed us to extract information from the full shape of our clustering measurements including smaller scales than in previous analyses. We performed extensive tests of this model using various N-body simulations and BOSS mock catalogues, showing that it can be used to extract cosmological information from our measurements of three clustering wedges for scales $s \gtrsim 20\,h^{-1}$ Mpc without introducing any significant systematic errors.

We used the information from our clustering measurements in combination with the latest CMB measurements from Planck and the JLA SN sample to constrain the parameters of the ΛCDM model and a number of its potential extensions, including more general dark energy models, non-flat universes, neutrino masses and possible deviations from the predictions of GR. Our results are completely consistent with the standard ΛCDM plus GR cosmological paradigm. When this model is extended by allowing one

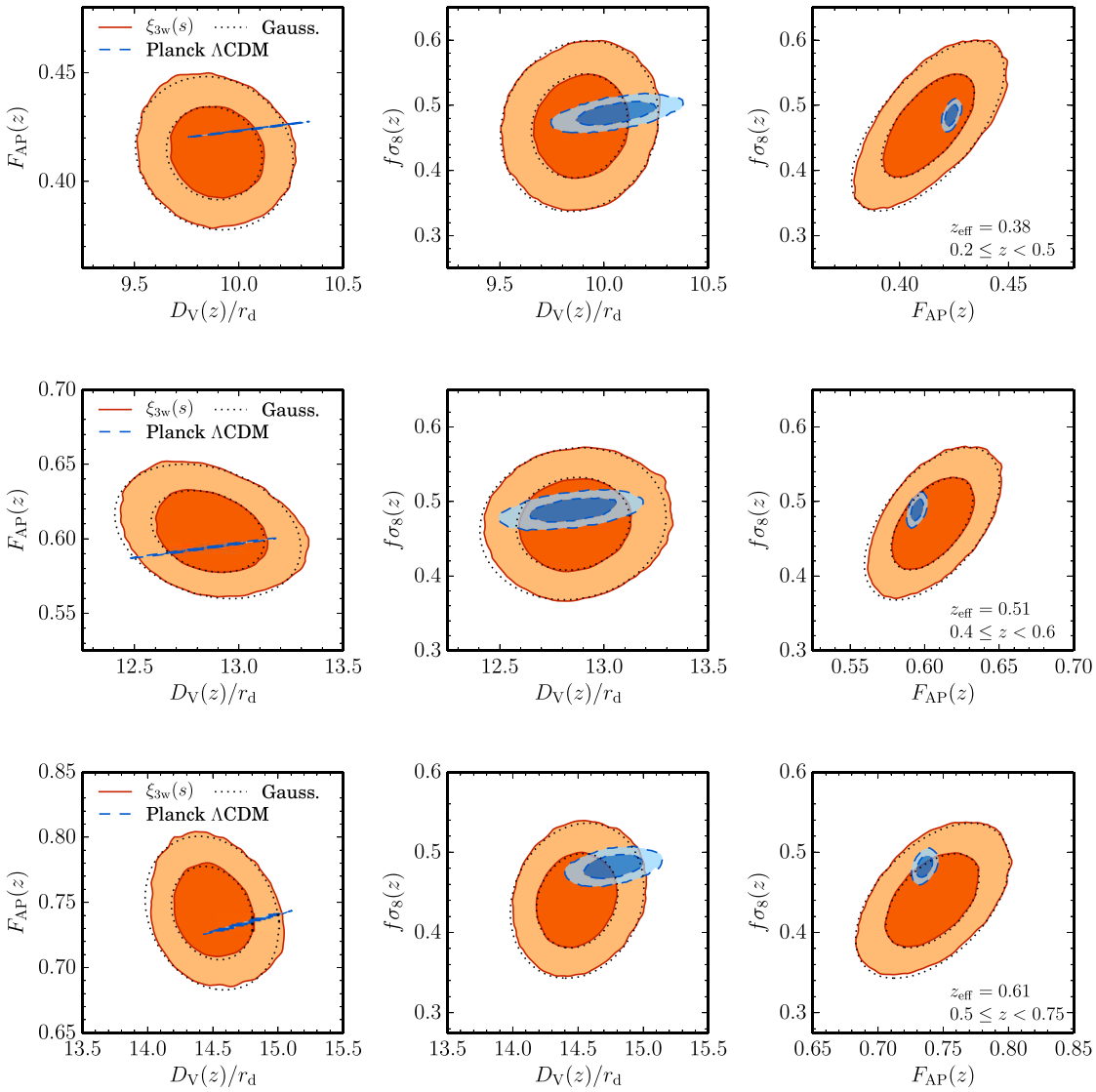

Figure 16. Two-dimensional 68 and 95 per cent marginalized constraints on $D_V(z)/r_d$, $F_{AP}(z)$ and $f\sigma_8(z)$. The solid lines show the results obtained from the measurements of the clustering wedges $\xi_{3w}(s)$ of the final BOSS combined sample in each of our three redshift bins. The dotted lines show the Gaussian approximation of these results using the mean values and covariance matrices of Tables 4 and 5. The dashed lines correspond to the constraints inferred from the Planck CMB measurements under the assumption of a ΛCDM model.

Table 4. Mean values and 68 per cent CL on $D_V(z)/r_d$, $F_{AP}(z)$ and $f\sigma_8(z)$ obtained from the clustering wedges $\xi_{3w}(s)$ of the final BOSS combined sample in each of our three redshift bins.

Parameter	$z_{eff} = 0.38$	$z_{eff} = 0.51$	$z_{eff} = 0.61$
$D_V(z)/r_d$	9.89 ± 0.15	12.86 ± 0.18	14.51 ± 0.21
$F_{AP}(z)$	0.413 ± 0.014	0.605 ± 0.018	0.742 ± 0.024
$f\sigma_8(z)$	0.468 ± 0.052	0.470 ± 0.041	0.439 ± 0.039

additional parameter to vary freely, the combination of the CMB data from Planck and our BOSS LSS measurements is enough to put tight constraints on the additional variable, with the SN data leading only to marginal improvements. The SN information is most useful when more than one additional parameter is included in the analysis, leading to final constraints in agreement with the canonical ΛCDM values. The full data set combination can constrain the dark energy equation-of-state parameter to $w_{DE} = -0.996 \pm 0.042$ when assumed time independent, with no indication of a departure from this value when it is allowed to evolve with redshift according to equation (32). The simultaneous variation of additional cosmological parameters does not affect this limit significantly. Our results are also completely consistent with the flat-Universe prediction from the most simple inflationary models, with $\Omega_k = -0.0007 \pm 0.0030$. We derive tight constraints on the total sum of neutrino masses to $\sum m_\nu < 0.25$ eV at 95 per cent CL. We also test the agreement of our clustering measurements with the predictions of GR by assuming the parametrization of equation (33) for the growth rate of cosmic structure and find $\gamma = 0.609 \pm 0.079$, in agreement with the GR value of $\gamma = 0.55$.

Of our companion papers based on the BOSS DR12 combined sample, the analysis of Grieb et al. (2016b) is the one more similar to ours. They use Fourier-space wedges measured by filtering out the information of Legendre multipoles $\ell > 4$ in the same redshift

Table 5. Covariance matrices associated with the constraints on $D_V(z)/r_d$, $F_{AP}(z)$ and $f\sigma_8(z)$ inferred from our MCMC fits to the clustering wedges of the final BOSS combined sample in each of our three redshift bins. The online files have the full numerical precision, which we recommend for parameter fits.

Parameter	$D_V(z)/r_d$	$F_{AP}(z)$	$f\sigma_8(z)$
	$0.2 < z < 0.5$, $z_{eff} = 0.38$		
$D_V(z)/r_d$	$2.309\,28 \times 10^{-2}$	$-2.201\,48 \times 10^{-4}$	$8.840\,51 \times 10^{-4}$
$F_{AP}(z)$	$-2.201\,48 \times 10^{-4}$	$2.005\,47 \times 10^{-4}$	$4.826\,76 \times 10^{-4}$
$f\sigma_8(z)$	$8.840\,51 \times 10^{-4}$	$4.826\,76 \times 10^{-4}$	$2.762\,87 \times 10^{-3}$
	$0.4 < z < 0.6$, $z_{eff} = 0.51$		
$D_V(z)/r_d$	$3.244\,93 \times 10^{-2}$	$-8.316\,65 \times 10^{-4}$	$7.009\,01 \times 10^{-4}$
$F_{AP}(z)$	$-8.316\,65 \times 10^{-4}$	$3.307\,09 \times 10^{-4}$	$4.028\,45 \times 10^{-4}$
$f\sigma_8(z)$	$7.009\,01 \times 10^{-4}$	$4.028\,45 \times 10^{-4}$	$1.689\,99 \times 10^{-3}$
	$0.5 < z < 0.75$, $z_{eff} = 0.61$		
$D_V(z)/r_d$	$4.253\,31 \times 10^{-2}$	$-9.324\,43 \times 10^{-4}$	$1.312\,94 \times 10^{-3}$
$F_{AP}(z)$	$-9.324\,43 \times 10^{-4}$	$5.626\,34 \times 10^{-4}$	$4.608\,68 \times 10^{-4}$
$f\sigma_8(z)$	$1.312\,94 \times 10^{-3}$	$4.608\,68 \times 10^{-4}$	$1.515\,96 \times 10^{-3}$

bins as in our analysis, which are also fitted using the model of non-linearities, bias and RSD described in Section 3. This is then the first time that the same model is applied in configuration and Fourier-space fits. A comparison of our results with those of Grieb et al. (2016b) shows excellent agreement, with both sets of measurements providing similar constraining power.

The information of our clustering measurements can be compressed into constraints on the parameter combinations $D_V(z)/r_d$, $F_{AP}(z)$ and $f\sigma_8(z)$ at the mean redshifts of each of our three redshift bins with their respective covariance matrices. These results are in excellent agreement with the predictions of the best-fitting ΛCDM model to the CMB measurements from Planck, highlighting the consistency between these data sets. Our results are combined with those of our companion papers into a final set of consensus constraints in Alam et al. (2016) using the methodology described in Sánchez et al. (2016).

Our results show that anisotropic clustering measurements have become one of the most powerful available cosmological probes. By exploiting the BAO and RSD signals imprinted in these measurements, the BOSS galaxy samples have significantly improved our knowledge of the basic cosmological parameters. The application of the methodology presented here to galaxy samples from future surveys such as the Dark Energy Spectroscopic Instrument (Levi et al. 2013) and the ESA space mission *Euclid* (Laureijs et al. 2011) will help to push our tests of the ΛCDM paradigm to even higher accuracies. A joint analysis of two-point statistics with higher order measurements such as the three-point correlation function or the bispectrum (Gil-Marín et al. 2015), a detailed study of RSDs on small scales including the impact of effects such as velocity or assembly bias (Reid et al. 2014), or the advancement of methods to reconstruct the underlying density field (Kitaura et al. 2016b) are strategies that could help us to further increase the information extracted from LSS data sets, which will continue shaping our understanding of cosmic history.

ACKNOWLEDGEMENTS

We thank the anonymous referee for his/her helpful comments and suggestions. AGS would like to thank Ximena Mazzalay for her invaluable help in the preparation of this manuscript. We would like to thank Riccardo Bolze, Daniel Farrow, Jiamin Hou and Francesco Montesano for useful discussions. AGS, JNG and SSA acknowledge support from the Trans-regional Collaborative Research Centre TR33 'The Dark Universe' of the German Research Foundation. RS was partially supported by NSF grant AST-1109432. CDV acknowledges financial support from the Spanish Ministry of Economy and Competitiveness (MINECO) under the 2011 and 2015 Severo Ochoa Programs SEV-2011-0187 and SEV-2015-0548, and grants AYA2013-46886 and AYA2014-58308. MV is partially supported by Programa de Apoyo a Proyectos de Investigación e Innovación Tecnológica (PAPITT) no. IA102516.

Funding for SDSS-III has been provided by the Alfred P. Sloan Foundation, the Participating Institutions, the National Science Foundation and the US Department of Energy.

SDSS-III is managed by the Astrophysical Research Consortium for the Participating Institutions of the SDSS-III Collaboration including the University of Arizona, the Brazilian Participation Group, Brookhaven National Laboratory, University of Cambridge, Carnegie Mellon University, University of Florida, the French Participation Group, the German Participation Group, Harvard University, the Instituto de Astrofisica de Canarias, the Michigan State/Notre Dame/JINA Participation Group, Johns Hopkins University, Lawrence Berkeley National Laboratory, Max Planck Institute for Astrophysics, Max Planck Institute for Extraterrestrial Physics, New Mexico State University, New York University, Ohio State University, Pennsylvania State University, University of Portsmouth, Princeton University, the Spanish Participation Group, University of Tokyo, University of Utah, Vanderbilt University, University of Virginia, University of Washington and Yale University.

Based on observations obtained with *Planck* (http://www.esa.int/Planck), an ESA science mission with instruments and contributions directly funded by ESA Member States, NASA and Canada.

REFERENCES

Aihara H. et al., 2011, ApJS, 193, 29
Alam S. et al., 2015, ApJS, 219, 12
Alam S. et al., 2016, MNRAS, preprint (arXiv:1607.03155)
Alcock C., Paczynski B., 1979, Nature, 281, 358
Amendola L., Quercellini C., Giallongo E., 2005, MNRAS, 357, 429
Anderson L. et al., 2012, MNRAS, 427, 3435
Anderson L. et al., 2014a, MNRAS, 439, 83
Anderson L. et al., 2014b, MNRAS, 441, 24
Baldauf T., Seljak U., Desjacques V., McDonald P., 2012, Phys. Rev. D, 86, 083540
Ballinger W. E., Peacock J. A., Heavens A. F., 1996, MNRAS, 282, 877
Barreira A., Sánchez A. G., Schmidt F., 2016, preprint (arXiv:1605.03965)
Baumann D., Nicolis A., Senatore L., Zaldarriaga M., 2012, J. Cosmol. Astropart. Phys., 7, 51
Bel J., Hoffmann K., Gaztañaga E., 2015, MNRAS, 453, 259
Bernardeau F., Crocce M., Scoccimarro R., 2008, Phys. Rev. D, 78, 103521
Bernardeau F., Crocce M., Scoccimarro R., 2012, Phys. Rev. D, 85, 123519
Bernardeau F., Taruya A., Nishimichi T., 2014, Phys. Rev. D, 89, 023502
Betoule M. et al., 2014, A&A, 568, A22
Beutler F. et al., 2014, MNRAS, 443, 1065
Beutler F. et al., 2016a, MNRAS, in press
Beutler F. et al., 2016b, preprint (arXiv:1607.03150)
Biagetti M., Desjacques V., Kehagias A., Riotto A., 2014, Phys. Rev. D, 90, 045022
Blake C., Glazebrook K., 2003, ApJ, 594, 665
Blake C. et al., 2011, MNRAS, 418, 1707
Bolton A. S. et al., 2012, AJ, 144, 144
Carlson J., Reid B., White M., 2013, MNRAS, 429, 1674
Carrasco J. J. M., Hertzberg M. P., Senatore L., 2012, J. High Energy Phys., 2012, 82
Catelan P., Lucchin F., Matarrese S., Porciani C., 1998, MNRAS, 297, 692

Catelan P., Porciani C., Kamionkowski M., 2000, MNRAS, 318, L39
Chan K. C., Scoccimarro R., Sheth R. K., 2012, Phys. Rev. D, 85, 083509
Chevallier M., Polarski D., 2001, Int. J. Mod. Phys. D, 10, 213
Chuang C.-H. et al., 2013, MNRAS, 433, 3559
Cole S. et al., 2005, MNRAS, 362, 505
Colless M. et al., 2001, MNRAS, 328, 1039
Colless M. et al., 2003, preprint (astro-ph/0306581)
Crocce M., Scoccimarro R., 2006, Phys. Rev. D, 73, 063519
Crocce M., Scoccimarro R., 2008, Phys. Rev. D, 77, 023533
Crocce M., Scoccimarro R., Bernardeau F., 2012, MNRAS, 427, 2537
Cuesta A. J. et al., 2016, MNRAS, 457, 1770
Davis M., Peebles P. J. E., 1983, ApJ, 267, 465
Dawson K. S. et al., 2013, AJ, 145, 10
Dodelson S., Schneider M. D., 2013, Phys. Rev. D, 88, 063537
Efstathiou G., Bond J. R., 1999, MNRAS, 304, 75
Eisenstein D. J., Hu W., 1998, ApJ, 496, 605
Eisenstein D. J. et al., 2005, ApJ, 633, 560
Eisenstein D. J., Seo H.-J., Sirko E., Spergel D. N., 2007, ApJ, 664, 675
Eisenstein D. J. et al., 2011, AJ, 142, 72
Feldman H. A., Kaiser N., Peacock J. A., 1994, ApJ, 426, 23
Font-Ribera A., McDonald P., Mostek N., Reid B. A., Seo H.-J., Slosar A., 2014, J. Cosmol. Astropart. Phys., 5, 023
Fry J. N., 1996, ApJ, 461, L65
Gil-Marín H. et al., 2015, MNRAS, 452, 1914
Grieb J. N., Sánchez A. G., Salazar-Albornoz S., Dalla Vecchia C., 2016a, MNRAS, 457, 1577
Grieb J. N. et al., 2016b, MNRAS, preprint (arXiv:1607.03143)
Gunn J. E. et al., 1998, AJ, 116, 3040
Gunn J. E. et al., 2006, AJ, 131, 2332
Guzzo L. et al., 2008, Nature, 451, 541
Hartlap J., Simon P., Schneider P., 2007, A&A, 464, 399
Hu W., Haiman Z., 2003, Phys. Rev. D, 68, 063004
Kaiser N., 1987, MNRAS, 227, 1
Kaufman G. M., 1967, Center for Operations Research and Econometrics Report No. 6710
Kazin E. A., Sánchez A. G., Blanton M. R., 2012, MNRAS, 419, 3223
Kitaura F.-S. et al., 2016a, MNRAS, 456, 4156
Kitaura F.-S., Ata M., Angulo R. E., Chuang C.-H., Rodríguez-Torres S., Monteagudo C. H., Prada F., Yepes G., 2016b, MNRAS, 457, L113
Landy S. D., Szalay A. S., 1993, ApJ, 412, 64
Laureijs R. et al., 2011, preprint (arXiv:1110.3193)
Levi M. et al., 2013, preprint (arXiv:1308.0847)
Lewis A., Bridle S., 2002, Phys. Rev. D, 66, 103511
Lewis A., Challinor A., Lasenby A., 2000, ApJ, 538, 473
Linder E. V., 2003, Phys. Rev. Lett., 90, 091301
Linder E. V., Cahn R. N., 2007, Astropart. Phys., 28, 481
McDonald P., 2006, Phys. Rev. D, 74, 103512
McDonald P., Roy A., 2009, J. Cosmol. Astropart. Phys., 8, 20
Maddox S. J., Efstathiou G., Sutherland W. J., Loveday J., 1990, MNRAS, 242, 43p
Manera M. et al., 2013, MNRAS, 428, 1036
Maraston C. et al., 2013, MNRAS, 435, 2764
Masters K. L. et al., 2011, MNRAS, 418, 1055
Matsubara T., 2004, ApJ, 615, 573
Meiksin A., White M., Peacock J. A., 1999, MNRAS, 304, 851
Nuza S. E. et al., 2013, MNRAS, 432, 743
Otten E. W., Weinheimer C., 2008, Rep. Prog. Phys., 71, 086201
Padmanabhan N., White M., 2008, Phys. Rev. D, 77, 123540
Padmanabhan N., Xu X., Eisenstein D. J., Scalzo R., Cuesta A. J., Mehta K. T., Kazin E., 2012, MNRAS, 427, 2132
Parejko J. K. et al., 2013, MNRAS, 429, 98
Parkinson D. et al., 2012, Phys. Rev. D, 86, 103518
Paz D. J., Sánchez A. G., 2015, MNRAS, 454, 4326
Percival W. J. et al., 2002, MNRAS, 337, 1068
Percival W. J. et al., 2010, MNRAS, 401, 2148
Percival W. J. et al., 2014, MNRAS, 439, 2531
Pietroni M., Mangano G., Saviano N., Viel M., 2012, J. Cosmol. Astropart. Phys., 1, 19
Planck Collaboration XVI, 2014, A&A, 571, A16
Planck Collaboration XIII, 2016, A&A, 594, A13
Pueblas S., Scoccimarro R., 2009, Phys. Rev. D, 80, 043504
Raccanelli A. et al., 2013, MNRAS, 436, 89
Reid B. A., White M., 2011, MNRAS, 417, 1913
Reid B. A. et al., 2012, MNRAS, 426, 2719
Reid B. A., Seo H.-J., Leauthaud A., Tinker J. L., White M., 2014, MNRAS, 444, 476
Reid B. et al., 2016, MNRAS, 455, 1553
Ross A. J. et al., 2016, MNRAS, 464, 1168
Saito S., Baldauf T., Vlah Z., Seljak U., Okumura T., McDonald P., 2014, Phys. Rev. D, 90, 123522
Salazar-Albornoz S. et al., 2016, MNRAS, preprint (arXiv:1607.03144)
Samushia L. et al., 2013, MNRAS, 429, 1514
Samushia L. et al., 2014, MNRAS, 439, 3504
Sánchez A. G., Baugh C. M., Percival W. J., Peacock J. A., Padilla N. D., Cole S., Frenk C. S., Norberg P., 2006, MNRAS, 366, 189
Sánchez A. G., Crocce M., Cabré A., Baugh C. M., Gaztañaga E., 2009, MNRAS, 400, 1643
Sánchez A. G. et al., 2012, MNRAS, 425, 415
Sánchez A. G. et al., 2013, MNRAS, 433, 1202
Sánchez A. G. et al., 2014, MNRAS, 440, 2692
Sánchez A. G. et al., 2016, MNRAS, preprint (arXiv:1607.03146)
Satpathy S. et al., 2016, MNRAS, preprint (arXiv:1607.03148)
Scoccimarro R., 2004, Phys. Rev. D, 70, 083007
Scoccimarro R., Frieman J., 1996, ApJS, 105, 37
Scoccimarro R., Couchman H. M. P., Frieman J. A., 1999, ApJ, 517, 531
Seo H. et al., 2010, ApJ, 720, 1650
Sheth R. K., Chan K. C., Scoccimarro R., 2013, Phys. Rev. D, 87, 083002
Shoji M., Jeong D., Komatsu E., 2009, ApJ, 693, 1404
Smee S. A. et al., 2013, AJ, 146, 32
Song Y.-S. et al., 2015, Phys. Rev. D, 92, 043522
Springel V., White S. D., Tormen G., Kauffmann G., 2001, MNRAS, 328, 726
Taruya A., Nishimichi T., Saito S., 2010, Phys. Rev. D, 82, 063522
Taruya A., Bernardeau F., Nishimichi T., Codis S., 2012, Phys. Rev. D, 86, 103528
Taruya A., Nishimichi T., Bernardeau F., 2013, Phys. Rev. D, 87, 083509
Taruya A., Koyama K., Hiramatsu T., Oka A., 2014, Phys. Rev. D, 89, 043509
Taylor A., Joachimi B., 2014, MNRAS, 442, 2728
Taylor A., Joachimi B., Kitching T., 2013, MNRAS, 432, 1928
Tegmark M. et al., 2004, ApJ, 606, 702
Thomas D. et al., 2013, MNRAS, 431, 1383
Wagner C., Müller V., Steinmetz M., 2008, A&A, 487, 63
Wang L., Reid B., White M., 2014, MNRAS, 437, 588
White M. et al., 2011, ApJ, 728, 126
White M., Tinker J. L., McBride C. K., 2014, MNRAS, 437, 2594
Wishart J., 1928, Biometrika, 20A, 32
Wyman M., Jennings E., Lima M., 2013, Phys. Rev. D, 88, 084029
York D. G. et al., 2000, AJ, 120, 1579
Zhang P., Liguori M., Bean R., Dodelson S., 2007, Phys. Rev. Lett., 99, 141302
Zheng Z., Coil A. L., Zehavi I., 2007, ApJ, 667, 760

APPENDIX A: DETAILS OF THE MODELLING OF THE TWO-DIMENSIONAL POWER SPECTRUM

In this appendix, we present a more detailed description of our model of non-linear evolution, bias and RSDs. The operators defined in Section 3.1.2 can be expressed in Fourier space as

$$\mathcal{G}_2(\boldsymbol{k}) = [\delta_{\rm D}]^k_{12}\,[(\widehat{k}_1\cdot\widehat{k}_2)^2 - 1]\,\theta(\boldsymbol{k}_1)\theta(\boldsymbol{k}_2) \tag{A1}$$

$$\equiv [\delta_{\rm D}]^k_{12}\,K(\boldsymbol{k}_1,\boldsymbol{k}_2)\,\theta(\boldsymbol{k}_1)\theta(\boldsymbol{k}_2), \tag{A2}$$

with $[\delta_{\rm D}]^k_n \equiv \delta_{\rm D}(\boldsymbol{k}-\boldsymbol{k}_n)$, $\boldsymbol{k}_{1\ldots n} \equiv \boldsymbol{k}_1+\cdots+\boldsymbol{k}_n$ and repeated Fourier arguments are understood to be integrated over. Using this equation, the cubic operator can be written as

$$\Delta_3\mathcal{G}(\boldsymbol{k}) = [\delta_{\rm D}]^k_{12}\,[(\widehat{k}_1\cdot\widehat{k}_2)^2-1]\,(\delta(\boldsymbol{k}_1)\delta(\boldsymbol{k}_2) \tag{A3}$$

$$-\theta(\boldsymbol{k}_1)\theta(\boldsymbol{k}_2)). \tag{A4}$$

Now, since in second-order perturbation theory

$$\delta^{(2)}(k)-\theta^{(2)}(k) = -\frac{2}{7}\mathcal{G}_2(\boldsymbol{k}), \tag{A5}$$

we have to leading order (and fully symmetrizing)

$$\begin{aligned}\Delta_3\mathcal{G}(\boldsymbol{k}) = &-\frac{4}{21}[\delta_{\rm D}]^k_{123}\,[K(\boldsymbol{k}_{12},\boldsymbol{k}_3)K(\boldsymbol{k}_1,\boldsymbol{k}_2)\\ &+K(\boldsymbol{k}_{23},\boldsymbol{k}_1)K(\boldsymbol{k}_2,\boldsymbol{k}_3)+K(\boldsymbol{k}_{31},\boldsymbol{k}_2)K(\boldsymbol{k}_3,\boldsymbol{k}_1)]\\ &\times\delta^{(1)}(\boldsymbol{k}_1)\delta^{(1)}(\boldsymbol{k}_2)\delta^{(1)}(\boldsymbol{k}_3),\end{aligned} \tag{A6}$$

in terms of the linear density fluctuations.

The galaxy auto power spectrum can be written as usual, to one-loop

$$\begin{aligned}P_{gg}(k) = &\,b_1^2P(k)+b_1b_2P_{b_1b_2}(k)+b_1\gamma_2P_{b_1\gamma_2}(k)\\ &+b_2^2\,P_{b_2b_2}(k)+b_2\gamma_2P_{b_2\gamma_2}(k)+\gamma_2^2P_{\gamma_2\gamma_2}(k)\\ &+b_1\gamma_3^-P_{b_1\gamma_3^-}(k)+P_{\rm noise}(k).\end{aligned} \tag{A7}$$

Each of these contributions is given by (in the following all powers inside integrands are linear)

$$P_{b_1b_2}(k) = \int 2F_2(\boldsymbol{k}-\boldsymbol{q},\boldsymbol{q})P(\boldsymbol{k}-\boldsymbol{q})P(q)\mathrm{d}^3q, \tag{A8}$$

$$\begin{aligned}P_{b_1\gamma_2}(k) &= P^{\rm mc}_{b_1\gamma_2}(k)+P^{\rm prop}_{b_1\gamma_2}(k)\\ &= \int 4F_2(\boldsymbol{k}-\boldsymbol{q},\boldsymbol{q})K(\boldsymbol{k}-\boldsymbol{q},\boldsymbol{q})P(\boldsymbol{k}-\boldsymbol{q})P(q)\mathrm{d}^3q\\ &\quad+8P(k)\int G_2(\boldsymbol{k},\boldsymbol{q})K(\boldsymbol{k}-\boldsymbol{q},\boldsymbol{q})P(q)\mathrm{d}^3q,\end{aligned} \tag{A9}$$

$$P_{b_2b_2}(k) = \frac{1}{2}\int P(\boldsymbol{k}-\boldsymbol{q})P(q)\mathrm{d}^3q, \tag{A10}$$

$$P_{b_2\gamma_2}(k) = \int 2K(\boldsymbol{k}-\boldsymbol{q},\boldsymbol{q})P(\boldsymbol{k}-\boldsymbol{q})P(q)\mathrm{d}^3q, \tag{A11}$$

$$P_{\gamma_2\gamma_2}(k) = \int 2K(\boldsymbol{k}-\boldsymbol{q},\boldsymbol{q})^2P(\boldsymbol{k}-\boldsymbol{q})P(q)\mathrm{d}^3q, \tag{A12}$$

$$P_{b_1\gamma_3^-}(k) = -2\,\frac{8}{21}P(k)\int 6K(\boldsymbol{k}-\boldsymbol{q},\boldsymbol{q})K(\boldsymbol{k},\boldsymbol{q})P(q)\mathrm{d}^3q. \tag{A13}$$

Out of these, there are two terms that can be reduced to 1D integrals, they are the propagator-type integrals,

$$\begin{aligned}P^{\rm prop}_{b_1\gamma_2}(k) = -P(k)\int\Bigg[&\frac{(k^2+q^2)(33k^4+14k^2q^2+33q^4)}{42\,k^2\,q^4}\\ &+\frac{(k^2-q^2)^2(11k^4+34k^2q^2+11q^4)}{56\,k^3\,q^5}\,ln\frac{(k-q)^2}{(k+q)^2}\Bigg]P(q)\mathrm{d}^3q,\end{aligned} \tag{A14}$$

and

$$\begin{aligned}P_{b_1\gamma_3^-}(k) = 2\,P(k)\int\Bigg[&\frac{(k^2+q^2)(3k^4-14k^2q^2+3q^4)}{21\,k^2\,q^4}\\ &+\frac{(k^2-q^2)^4}{28\,k^3\,q^5}\ln\frac{(k-q)^2}{(k+q)^2}\Bigg]P(q)\mathrm{d}^3q.\end{aligned} \tag{A15}$$

The term P_{b2b2} does not reduce to zero at low-k; therefore, we renormalize that limit as (McDonald 2006)

$$P_{b_2b_2}(k) = \frac{1}{2}\int\left(1-\frac{P(q)}{P(\boldsymbol{k}-\boldsymbol{q})}\right)P(\boldsymbol{k}-\boldsymbol{q})P(q)\mathrm{d}^3q, \tag{A16}$$

which now reduces to zero as k^2. This constant low-k limit enters as an additional shot noise

$$P_{\rm noise}(k) = \frac{b_2^2}{2}\int P(q)^2\mathrm{d}^3q; \tag{A17}$$

in practice, we marginalize over shot noise for power spectrum analysis (Grieb et al. 2016a), and we can ignore shot noise renormalization for the two-point function analysis.

Similarly, we have to one-loop for the cross spectrum between galaxy fluctuations and velocity divergence that

$$\begin{aligned}P_{g\theta}(k) = &\,b_1P_{\delta\theta}(k)+b_2P_{b_2}(k)+\gamma_2P_{\gamma_2}(k)\\ &+\gamma_3^-P_{\gamma_3^-}(k),\end{aligned} \tag{A18}$$

where

$$P_{b_2}(k) = \int G_2(\boldsymbol{k}-\boldsymbol{q},\boldsymbol{q})P(\boldsymbol{k}-\boldsymbol{q})P(q)\mathrm{d}^3q, \tag{A19}$$

$$\begin{aligned}P_{\gamma_2}(k) &= P^{\rm mc}_{\gamma_2}(k)+P^{\rm prop}_{\gamma_2}(k),\\ &= \int 2\,G_2(\boldsymbol{k}-\boldsymbol{q},\boldsymbol{q})K(\boldsymbol{k}-\boldsymbol{q},\boldsymbol{q})P(\boldsymbol{k}-\boldsymbol{q})P(q)\mathrm{d}^3q\\ &\quad+4\,P(k)\int G_2(\boldsymbol{k},\boldsymbol{q})K(\boldsymbol{k}-\boldsymbol{q},\boldsymbol{q})P(q)\mathrm{d}^3q,\end{aligned} \tag{A20}$$

and note that $P^{\rm prop}_{\gamma_2} = P^{\rm prop}_{b_1\gamma_2}/2$ and $P_{\gamma_3^-} = P_{b_1\gamma_3^-}/2$.

APPENDIX B: CONSTRAINTS ON THE ΛCDM PARAMETER SPACE

In this appendix, we summarize the constraints on the cosmological parameters of the ΛCDM model analysed in Section 4.2. Table B1

Table B1. Marginalized 68 per cent constraints on the cosmological parameters of the standard ΛCDM model, obtained using different combinations of the data sets described in Section 4.1.

	Planck + BOSS ξ_{3w}	Planck + BOSS ξ_{3w} + SN
Main parameters		
$100\,\omega_{\rm b}$	2.228 ± 0.020	2.229 ± 0.020
$100\,\omega_{\rm c}$	$11.81^{+0.13}_{-0.16}$	$11.80^{+0.13}_{-0.15}$
$10^4 \times \theta_{\rm MC}$	104.104 ± 0.042	104.107 ± 0.042
$n_{\rm s}$	0.9680 ± 0.0048	0.9682 ± 0.0048
$\ln(10^{10}A_{\rm s})$	3.078 ± 0.033	3.078 ± 0.033
Derived parameters		
$100\Omega_{\rm DE}$	$69.46^{+0.95}_{-0.79}$	$69.52^{+0.91}_{-0.76}$
$100\Omega_{\rm m}$	$30.54^{+0.79}_{-0.95}$	$30.48^{+0.76}_{-0.91}$
h	$0.6798^{+0.0070}_{-0.0062}$	$0.6803^{+0.0067}_{-0.0059}$
σ_8	0.820 ± 0.014	0.820 ± 0.014
S_8	$0.827^{+0.018}_{-0.020}$	0.826 ± 0.018

list the 68 per cent confidence limits obtained in this parameter space. The upper section of the table lists the constraints on the main parameters included in the fits, while the lower section contains the results on the parameters derived from the first set.

[1]*Max-Planck-Institut für extraterrestrische Physik, Postfach 1312, Giessenbachstr., D-85741 Garching, Germany*
[2]*Center for Cosmology and Particle Physics, Department of Physics, New York University, New York, NY 10003, USA*
[3]*Institut de Ciències de l'Espai, IEEC-CSIC, Campus UAB, Carrer de Can Magrans, s/n, E-08193 Bellaterra, Barcelona, Spain*
[4]*Universitäts-Sternwarte München, Ludwig-Maximilians-Universität München, Scheinerstrasse 1, D-81679 Munich, Germany*
[5]*Instituto de Astrofísica de Canarias, C/ Vía Láctea s/n, E-38205 La Laguna, Tenerife, Spain*
[6]*Departamento de Astrofísica, Universidad de La Laguna, Av. del Astrofísico Francisco Sánchez s/n, E-38206 La Laguna, Tenerife, Spain*
[7]*Institute of Cosmology and Gravitation, Dennis Sciama Building, University of Portsmouth, Portsmouth PO1 3FX, UK*
[8]*Lawrence Berkeley National Laboratory, 1 Cyclotron Road, Berkeley, CA 94720, USA*
[9]*Department of Physics and Astronomy, University of Utah, 115 S 1400 E, Salt Lake City, UT 84112, USA*
[10]*Instituto de Física Teórica, UAM/CSIC, Universidad Autónoma de Madrid, Cantoblanco, E-28049 Madrid, Spain*
[11]*Leibniz-Institut für Astrophysik Potsdam, An der Sternwarte 16, D-14482 Potsdam, Germany*
[12]*Harvard–Smithsonian Center for Astrophysics, 60 Garden St, Cambridge, MA 02138, USA*
[13]*Departments of Physics and Astronomy, University of California, Berkeley, CA 94720, USA*
[14]*Department of Chemistry and Physics, King's College, 133 North River St, Wilkes Barre, PA 18711, USA*
[15]*Campus of International Excellence UAM+CSIC, Cantoblanco, E-28049 Madrid, Spain*
[16]*Instituto de Astrofísica de Andalucía, CSIC, Glorieta de la Astronomía, E-18080 Granada, Spain*
[17]*Departamento de Física Teórica, Universidad Autónoma de Madrid, Cantoblanco, E-28049 Madrid, Spain*
[18]*Center for Cosmology and Astro-Particle Physics, Ohio State University, Columbus, OH 43210, USA*
[19]*Kansas State University, Manhattan, KS 66506, USA*
[20]*National Abastumani Astrophysical Observatory, Ilia State University, 2A Kazbegi Ave, GE-1060 Tbilisi, Georgia*
[21]*Department of Physics and Astronomy, Ohio University, 251B Clippinger Labs, Athens, OH 45701, USA*
[22]*School of Physics and Astronomy, University of St Andrews, North Haugh, St Andrews KY16 9SS, UK*
[23]*Instituto de Física, Universidad Nacional Autónoma de México, Apdo. Postal 20-364, 01000 México, D.F., Mexico*
[24]*Department of Physics, Carnegie Mellon University, 5000 Forbes Ave, Pittsburgh, PA 15217, USA*
[25]*McWilliams Center for Cosmology, Carnegie Mellon University, 5000 Forbes Ave, Pittsburgh, PA 15217, USA*
[26]*National Astronomy Observatories, Chinese Academy of Science, Beijing 100012, People's Republic of China*

This paper has been typeset from a TEX/LATEX file prepared by the author.